

# Quantum Monte Carlo calculations of $A = 8$ nuclei

R. B. Wiringa\* and Steven C. Pieper†

*Physics Division, Argonne National Laboratory, Argonne, IL 60439*

J. Carlson‡

*Theoretical Division, Los Alamos National Laboratory, Los Alamos New Mexico 87545*

V. R. Pandharipande§

*Physics Department, University of Illinois at Urbana-Champaign, 1110 West Green St., Urbana, Illinois 61801*

(October 25, 2018)

## Abstract

We report quantum Monte Carlo calculations of ground and low-lying excited states for  $A = 8$  nuclei using a realistic Hamiltonian containing the Argonne  $v_{18}$  two-nucleon and Urbana IX three-nucleon potentials. The calculations begin with correlated eight-body wave functions that have a filled  $\alpha$ -like core and four p-shell nucleons  $LS$ -coupled to the appropriate ( $J^\pi; T$ ) quantum numbers for the state of interest. After optimization, these variational wave functions are used as input to a Green's function Monte Carlo calculation made with a new constrained path algorithm. We find that the Hamiltonian produces a  ${}^8\text{Be}$  ground state that is within 2 MeV of the experimental resonance, but the other eight-body energies are progressively worse as the neutron-proton asymmetry increases. The  ${}^8\text{Li}$  ground state is stable against breakup into subclusters, but the  ${}^8\text{He}$  ground state is not. The excited state spectra are in fair agreement with experiment, with both the single-particle behavior of  ${}^8\text{He}$  and  ${}^8\text{Li}$  and the collective rotational behavior of  ${}^8\text{Be}$  being reproduced. We also examine energy differences in the  $T = 1$  and 2 isomultiplets and isospin-mixing matrix elements in the excited states of  ${}^8\text{Be}$ . Finally, we present densities, momentum distributions, and studies of the intrinsic shapes of these nuclei, with  ${}^8\text{Be}$  exhibiting a definite  $2\alpha$  cluster structure.

PACS numbers: 21.10.-k, 21.45.+v, 21.60.Ka, 27.20.+n

Typeset using REVTeX

## I. INTRODUCTION

The  $A = 8$  nuclei have many interesting properties that we would like to understand on the basis of the bare interactions between individual nucleons. The three strong-stable nuclei,  ${}^8\text{He}$ ,  ${}^8\text{Li}$ , and  ${}^8\text{B}$ , decay by weak processes with half-lives of  $\lesssim 1$  second down to  ${}^8\text{Be}$ , which then immediately fissions to two  ${}^4\text{He}$  nuclei; thus there are no long-lived  $A = 8$  nuclei. These facts have tremendous consequences for the nature of the universe we live in: they make the production of elements beyond  $A = 7$  in the early universe very difficult and help give stars like the sun a long stable lifetime. The ground and excited states of the  $A = 8$  nuclei also provide a very sensitive testing ground for models of nuclear forces. In particular,  ${}^8\text{He}$  is the most neutron-rich strong-stable nucleus, and thus an ideal place to study the isospin dependence of the three-nucleon force. The  $T = 1, 2$  isomultiplets are also a good place to look at charge-independence breaking, while some excited states in  ${}^8\text{Be}$  display significant isospin mixing.

Previously we have reported variational Monte Carlo (VMC) and Green's function Monte Carlo (GFMC) calculations for the  $A = 6, 7$  nuclei [1]. In this paper we extend these calculations to the ground and excited states of  $A = 8$  nuclei. (Some preliminary  $A = 8$  results were given in a number of conference proceedings [2].) We first construct a trial function,  $\Psi_T$ , with the proper ( $J^\pi; T$ ) quantum numbers and antisymmetry, and optimize the energy expectation value. We then use  $\Psi_T$  as the starting point for a GFMC calculation, which projects out the exact lowest-energy state by the Euclidean propagation  $\Psi_0 = \lim_{\tau \rightarrow \infty} \exp[-(H - E_0)\tau]\Psi_T$ . We believe the resulting energy estimates are accurate to 1 to 2% of the binding energy in most cases.

In our previous work, the Argonne  $v_{18}$  plus Urbana IX Hamiltonian was fairly successful in generating the excitation spectra of the  $A = 6, 7$  nuclei, but did not give quite enough binding in the lithium isotopes, while  ${}^6\text{He}$  was unstable against breakup. One of our main goals in studying the  $A = 8$  nuclei is to continue to test the Hamiltonian, and lay the ground work for studies of more sophisticated and accurate three-nucleon forces. The Hamiltonian is reviewed in Sec. II. The variational wave functions and calculations are described in Sec. III. Our GFMC calculations make use of a new, more efficient algorithm called constrained-path propagation, which is described in Sec. IV. Results for the ground-state energies, excitation spectra, isomultiplet differences, and isospin-mixing matrix elements are given in Sec. V. In Sec. VI we present various density distributions, and in Sec. VII we discuss the intrinsic shapes of these nuclei. Our conclusions are given in Sec. VIII.

## II. HAMILTONIAN

These calculations all use the same realistic Hamiltonian, which includes a nonrelativistic one-body kinetic energy, the Argonne  $v_{18}$  two-nucleon potential [3] and the Urbana IX three-nucleon potential [4]:

$$H = \sum_i K_i + \sum_{i < j} v_{ij} + \sum_{i < j < k} V_{ijk} . \quad (2.1)$$

The kinetic energy operator has charge-independent (CI) and charge-symmetry-breaking (CSB) components, the latter due to the difference in proton and neutron masses,

$$K_i = K_i^{CI} + K_i^{CSB} \equiv -\frac{\hbar^2}{4} \left( \frac{1}{m_p} + \frac{1}{m_n} \right) \nabla_i^2 - \frac{\hbar^2}{4} \left( \frac{1}{m_p} - \frac{1}{m_n} \right) \tau_{zi} \nabla_i^2 . \quad (2.2)$$

The Argonne  $v_{18}$  model [3] is one of a class of new, highly accurate  $NN$  potentials that fit both  $pp$  and  $np$  scattering data up to 350 MeV with a  $\chi^2$ /datum near 1. The potential can be written as a sum of electromagnetic and one-pion-exchange terms and a shorter-range phenomenological part:

$$v_{ij} = v_{ij}^\gamma + v_{ij}^\pi + v_{ij}^R . \quad (2.3)$$

The electromagnetic terms include one- and two-photon-exchange Coulomb interactions, vacuum polarization, Darwin-Foldy, and magnetic moment terms, with appropriate proton and neutron form factors. The one-pion-exchange part of the potential includes the charge-dependent (CD) terms due to the difference in neutral and charged pion masses. The shorter-range part has about 40 parameters which are adjusted to fit the  $pp$  and  $np$  scattering data, the deuteron binding energy, and also the  $nn$  scattering length. The one-pion-exchange and the remaining phenomenological part of the potential can be written as a sum of eighteen operators,

$$v_{ij}^\pi + v_{ij}^R = \sum_{p=1,18} v_p(r_{ij}) O_{ij}^p . \quad (2.4)$$

The first fourteen are charge-independent,

$$O_{ij}^{p=1,14} = [1, \sigma_i \cdot \sigma_j, S_{ij}, \mathbf{L} \cdot \mathbf{S}, \mathbf{L}^2, \mathbf{L}^2 \sigma_i \cdot \sigma_j, (\mathbf{L} \cdot \mathbf{S})^2] \otimes [1, \tau_i \cdot \tau_j] , \quad (2.5)$$

and the last four,

$$O_{ij}^{p=15,18} = [1, \sigma_i \cdot \sigma_j, S_{ij}] \otimes T_{ij}, \tau_{zi} + \tau_{zj} , \quad (2.6)$$

break charge independence. We will refer to the potential from the  $p = 15 - 17$  terms as  $v^{CD}$  and from the  $p = 18$  term as  $v^{CSB}$ . We note that in the context of isospin symmetry the CI, CSB and CD terms are respectively isoscalar, isovector and isotensor.

The two-nucleon potential is supplemented by a three-nucleon interaction from the Urbana series of models [5], including both long-range two-pion exchange and a short-range phenomenological component:

$$V_{ijk} = V_{ijk}^{2\pi} + V_{ijk}^R . \quad (2.7)$$

The two-pion-exchange term can be expressed simply as a sum of anticommutator and commutator terms,

$$V_{ijk}^{2\pi} = \sum_{cyclic} V_{ij;k}^{2\pi,A} + V_{ij;k}^{2\pi,C} . \quad (2.8)$$

Here

$$V_{ij;k}^{2\pi,A} = A_{2\pi} \{ X_{ik}^\pi, X_{jk}^\pi \} \{ \tau_i \cdot \tau_k, \tau_j \cdot \tau_k \} , \quad (2.9)$$

and

$$V_{ij;k}^{2\pi,C} = \frac{1}{4} A_{2\pi} [X_{ik}^\pi, X_{jk}^\pi] [\tau_i \cdot \tau_k, \tau_j \cdot \tau_k] , \quad (2.10)$$

with  $X_{ij}^\pi = Y(r_{ij})\sigma_i \cdot \sigma_j + T(r_{ij})S_{ij}$  as the basic one-pion exchange operator. The  $V_{ijk}^R$  has no spin-isospin dependence, and in the Urbana model IX [4] its strength and  $A_{2\pi}$  are adjusted to reproduce the binding energy of  ${}^3\text{H}$  and give a reasonable saturation density in nuclear matter when used with Argonne  $v_{18}$ .

The CD and CSB terms in  $H$  are fairly weak, so we can treat them conveniently as a first-order perturbation and use a wave function of good isospin, which is significantly more compact. Also, direct GFMC calculations with the spin-dependent terms that involve the square of the momentum operator can have large statistical fluctuations, as discussed in Ref. [1]. Thus we construct the GFMC propagator with a simpler isoscalar Hamiltonian,

$$H' = \sum_i K_i^{CI} + \sum_{i < j} v'_{ij} + \sum_{i < j < k} V'_{ijk} , \quad (2.11)$$

where  $v'_{ij}$  is defined as

$$v'_{ij} = \sum_{p=1,8} v'_p(r_{ij}) O_{ij}^p + v'_C(r_{ij}) . \quad (2.12)$$

The interaction  $v'_{ij}$  has only eight operator terms, with operators  $[1, \sigma_i \cdot \sigma_j, S_{ij}, \mathbf{L} \cdot \mathbf{S}] \otimes [1, \tau_i \cdot \tau_j]$ , chosen such that it equals the isoscalar part of the full interaction in all  $S$  and  $P$  waves as well as in the  ${}^3D_1$  wave and its coupling to the  ${}^3S_1$ . The isoscalar part of the  $pp$  Coulomb interaction,  $v'_C$ , is also included in  $H'$ . Detailed expressions are given in Ref. [1]. The  $v'_{ij}$  is a little more attractive than  $v_{ij}$ , so we compensate by using a  $V'_{ijk}$  that is adjusted to keep  $\langle H' \rangle \approx \langle H \rangle$ ; this should help prevent the GFMC propagation from producing excessively large densities due to overbinding. The small contribution of  $(H - H')$  is calculated perturbatively.

### III. VARIATIONAL MONTE CARLO

The variational method can be used to obtain approximate solutions to the many-body Schrödinger equation,  $H\Psi = E\Psi$ , for a wide range of nuclear systems, including few-body nuclei, light closed-shell nuclei, nuclear matter, and neutron stars [6]. A suitably parameterized wave function,  $\Psi_V$ , is used to calculate an upper bound to the exact ground-state energy,

$$E_V = \frac{\langle \Psi_V | H | \Psi_V \rangle}{\langle \Psi_V | \Psi_V \rangle} \geq E_0 . \quad (3.1)$$

The parameters in  $\Psi_V$  are varied to minimize  $E_V$ , and the lowest value is taken as the approximate ground-state energy.

Upper bounds to excited states are also obtainable, either from standard VMC calculations if they have different quantum numbers from the ground state, or from small-basis diagonalizations if they have the same quantum numbers. The corresponding  $\Psi_V$  can then be used to calculate other properties, such as electromagnetic form factors [7] and spectroscopic factors [8], or it can be used as the starting point for a Green's function Monte Carlo

calculation. In this section we first describe our *ansatz* for  $\Psi_V$  for the  $A = 8$  nuclei and then briefly review how the expectation value, Eq. (3.1), is evaluated and the parameters of  $\Psi_V$  are fixed.

### A. Wave Function

Our best variational wave function for the nuclei studied here has the form [9]

$$|\Psi_V\rangle = \left[ 1 + \sum_{i < j < k} (U_{ijk} + U_{ijk}^{TNI}) + \sum_{i < j} U_{ij}^{LS} \right] |\Psi_P\rangle , \quad (3.2)$$

where the pair wave function,  $\Psi_P$ , is given by

$$|\Psi_P\rangle = \mathcal{S} \prod_{i < j} (1 + U_{ij}) |\Psi_J\rangle . \quad (3.3)$$

The  $U_{ij}$ ,  $U_{ij}^{LS}$ ,  $U_{ijk}$ , and  $U_{ijk}^{TNI}$  are noncommuting two- and three-nucleon correlation operators, and the  $\mathcal{S}$  is a symmetrization operator. The  $U_{ij}$  includes spin, isospin, and tensor operators, while the  $U_{ij}^{LS}$  has spin-orbit operators, reflecting the operator structure of the two-nucleon interaction, Eq. (2.4). The  $U_{ijk}$  is a nontrivial operator in spin-isospin space also induced by  $v_{ij}$ , while the  $U_{ijk}^{TNI}$  reflects the structure of the three-nucleon interaction. All these correlations are discussed fully in Refs. [1,9,10]. The two-body correlations are generated by the solution of coupled differential equations with embedded variational parameters. We have found that the parameters optimized for the  $\alpha$ -particle are near optimal for use in the light p-shell nuclei. Likewise, the best parameters for the three-body correlations are remarkably constant for different s- and p-shell nuclei, so they have not been changed from the previous work.

The form of the totally antisymmetric Jastrow wave function,  $\Psi_J$ , depends on the nuclear state under investigation. For s-shell nuclei we use the simple form

$$|\Psi_J\rangle = \prod_{i < j < k} f_{ijk}^c \prod_{i < j} f_c(r_{ij}) |\Phi_A(JMTT_3)\rangle . \quad (3.4)$$

Here  $f_c(r_{ij})$  and  $f_{ijk}^c$  are central two- and three-body correlation functions and for the  $\alpha$ -particle,

$$|\Phi_4(0000)\rangle = \mathcal{A} |p \uparrow p \downarrow n \uparrow n \downarrow\rangle . \quad (3.5)$$

The Jastrow wave function for the light p-shell nuclei is significantly more complicated due to the requirements of antisymmetry. Expressions for  $A = 6, 7$  nuclei are given in Ref. [1]; the present  $\Psi_J$  is a straightforward extension. We use  $LS$  coupling to obtain the desired  $JM$  value of a given state, as suggested by standard shell-model studies [11]. We also need to specify the spatial symmetry  $[n]$  of the angular momentum coupling of four p-shell nucleons [12]. Different possible  $LS[n]$  combinations lead to multiple components in the Jastrow wave function. We allow for the possibility that the central correlations  $f_c(r_{ij})$  could depend upon the shells ( $s$  or  $p$ ) occupied by the particles and on the  $LS[n]$  coupling. The Jastrow wave function is taken as

$$|\Psi_J\rangle = \mathcal{A} \{ \prod_{i < j < k \leq 4} f_{ijk}^c \prod_{i < j \leq 4} f_{ss}(r_{ij}) \prod_{k \leq 4} f_{sp}(r_{k5}) f_{sp}(r_{k6}) f_{sp}(r_{k7}) f_{sp}(r_{k8}) \\ \sum_{LS[n]} \left( \beta_{LS[n]} \prod_{5 \leq l < m \leq 8} f_{pp}^{[n]}(r_{lm}) |\Phi_8(LS[n]JMTT_3)_{1234:5678}\rangle \right) \} . \quad (3.6)$$

The operator  $\mathcal{A}$  indicates an antisymmetric sum over all possible partitions of the eight particles into 4 s-shell and 4 p-shell ones. For the two-body correlations we use  $f_{ss}(r) = f_c(r)$  from the  ${}^4\text{He}$  wave function, while

$$f_{sp}(r) = f_c(r) + c_{sp}(1 - \exp[-(r/d_{sp})^2]) , \quad (3.7)$$

$$(3.8)$$

and

$$f_{pp}^{[n]}(r) = f_c(r) + c_{pp}^{[n]}(1 - \exp[-(r/d_{pp})^2]) , \quad (3.9)$$

where we have supplemented the  $f_c(r)$  with a long-range tail. The  $c_{sp}$ ,  $d_{sp}$ , etc., are variational parameters, whose values are given in Table I. For the three-body correlations, our best present trial function has the  $f_{ijk}^c$  acting only within the s-shell.

The  $LS[n]$  components of the single-particle wave function are given by:

$$|\Phi_8(LS[n]JMTT_3)_{1234:5678}\rangle = |\Phi_4(0000)_{1234} \phi_p^{LS}(R_{\alpha 5}) \phi_p^{LS}(R_{\alpha 6}) \phi_p^{LS}(R_{\alpha 7}) \phi_p^{LS}(R_{\alpha 8}) \\ \{ [Y_{1m_l}(\Omega_{\alpha 5}) Y_{1m_l'}(\Omega_{\alpha 6}) Y_{1m_l''}(\Omega_{\alpha 7}) Y_{1m_l'''}(\Omega_{\alpha 8})]_{LM_L} \\ \times [\chi_5(\frac{1}{2}m_s) \chi_6(\frac{1}{2}m_s') \chi_7(\frac{1}{2}m_s'') \chi_8(\frac{1}{2}m_s''')]_{SM_S} \}_{JM} \\ \times [\nu_5(\frac{1}{2}t_3) \nu_6(\frac{1}{2}t_3') \nu_7(\frac{1}{2}t_3'') \nu_8(\frac{1}{2}t_3''')]_{TT_3} \rangle . \quad (3.10)$$

The  $\phi_p^{LS}(R_{\alpha k})$  are  $p$ -wave solutions of a particle of reduced mass  $\frac{4}{5}m_N$  in an effective  $\alpha$ - $N$  potential:

$$V_{\alpha N}(r) = V_{\alpha N}^{WS}(r) + V_{\alpha N}^C(r) . \quad (3.11)$$

They are functions of the distance between the center of mass of the  $\alpha$  core (which contains particles 1-4 in this partition) and nucleon  $k$ , and again may be different for different  $LS$  components. For each state considered in the present work, we have used bound-state asymptotic conditions for the  $\phi_p^{LS}$ , even if the state is particle unstable. The Woods-Saxon potential

$$V_{\alpha N}^{WS}(r) = V_p^{LS} [1 + \exp(\frac{r - R_p}{a_p})]^{-1} , \quad (3.12)$$

has variational parameters  $V_p^{LS}$ ,  $R_p$ , and  $a_p$  whose values are given in Table I. The Coulomb potential is obtained by folding over nuclear form factors:

$$V_{\alpha N}^C(r) = 2Q \frac{e^2}{r} \{ 1 - \frac{1}{2} \exp(-x_\alpha) [2 + x_\alpha + \frac{4}{1 - y^2}] [1 - y^{-2}]^{-2} \\ - \frac{1}{2} \exp(-x_p) [2 + x_p + \frac{4}{1 - y^{-2}}] [1 - y^2]^{-2} \} . \quad (3.13)$$

Here  $x_\alpha = \sqrt{12}r/r_\alpha$ ,  $x_p = \sqrt{12}r/r_p$ , and  $y = r_\alpha/r_p$ , with the charge radii  $r_\alpha = 1.65$  fm and  $r_p = 0.81$  fm. This additional potential term can be used with strength  $Q = 0$ ,  $\frac{1}{4}$ , or  $\frac{1}{2}$  for  ${}^8\text{He}$ ,  ${}^8\text{Li}$ , or  ${}^8\text{Be}$ , respectively, corresponding to the average Coulomb interaction between the  $\alpha$  core and a p-shell nucleon. The wave function is translationally invariant, hence there is no spurious center of mass motion.

The experimental spectra for  $A = 8$  nuclei [13] are shown in Fig. 1. The ground state of  ${}^8\text{He}$  is strong stable, but decays by  $\beta^-$  emission with a half life of 119 ms. One excited state is identified at  $3.59 \pm 0.05$  MeV [14], above the threshold for decay to  ${}^6\text{He} + 2n$ . In the shell model, the  $(J^\pi; T) = (0^+; 2)$  ground state is predominantly a  ${}^{2S+1}L[n] = {}^1S[22]$  state, where we use spectroscopic notation to denote the total  $L$  and  $S$  and the Young pattern  $[n]$  to indicate the spatial symmetry. The  $(2^+; 2)$  first excited state is predominantly a  ${}^1D[22]$  state. We also allow for possible  ${}^3P[211]$  admixtures, which are the only other available configurations in the p-shell, in our  $\Psi_J$ . After other parameters in the trial function have been optimized, we make a series of calculations in which the  $\beta_{LS[n]}$  may be different in the left- and right-hand-side wave functions to obtain the diagonal and off-diagonal matrix elements of the Hamiltonian and the corresponding normalizations and overlaps. We diagonalize the resulting matrices to find the  $\beta_{LS[n]}$  eigenvectors. The shell-model wave functions are orthonormal, but the correlated  $\Psi_V$  are not. Hence the diagonalizations use generalized eigenvalue routines including overlap matrices. We also calculate the position of the three predominantly  ${}^3P[211]$  states, with  $(J^\pi; T) = (2^+; 2)$ ,  $(1^+; 2)$ , and  $(0^+; 2)$ ; none of these have been identified experimentally. The normalized  $\beta_{LS[n]}$  for these different states are given in Table II.

The ground state of  ${}^8\text{Li}$  is a strong stable  $(2^+; 1)$  state that decays by  $\beta^-$  emission with a half life of 838 ms, and is predominantly  ${}^3P[31]$  in character. The  $(1^+; 1)$  first excited state at 0.98 MeV excitation is also strong stable with a 12 fs  $\gamma$ -decay, and is primarily a mix of  ${}^{1,3}P[31]$  configurations. The  $(3^+; 1)$  second excited state at 2.26 MeV is just above the threshold for breakup into  ${}^7\text{Li} + n$  and is fairly narrow with a width of 33 keV, decaying by both  $\gamma$  and  $n$  emission. A number of higher states have been identified, most having fairly large widths. Two special cases are the  $(4^+; 1)$  stretched state at 6.53 MeV excitation with a width of 35 keV, which can only come from the  ${}^3F[31]$  p-shell configuration, and the  $(0^+; 2)$  isobaric analog of  ${}^8\text{He}$  that occurs at 10.82 MeV with a width less than 12 keV. The possible p-shell components in the  $T = 1$  states include the  ${}^{1,3}P[31]$ ,  ${}^{1,3}D[31]$ ,  ${}^{1,3}F[31]$ ,  ${}^3S[22]$ ,  ${}^3D[22]$ , and  ${}^{1,3,5}P[211]$  configurations. We include all but the lowest-symmetry [211] components in our  $\Psi_J$  and calculate all possible first, second and some third states of given  $(J^\pi; T)$  through the diagonalization procedure discussed above. Table III gives a summary of the  $\beta_{LS[n]}$  amplitudes.

The  $(0^+; 0)$  ground state of  ${}^8\text{Be}$  is 92 keV above the threshold for breakup into two  $\alpha$ -particles, with a width of only 7 eV; it is an almost pure  ${}^1S[4]$  configuration. The first and second excited states are very broad: a  $(2^+; 0)$   ${}^1D[4]$  state at 3.04 MeV and a  $(4^+; 0)$   ${}^1G[4]$  state at 11.4 MeV — the spacing of an almost rigid rotor. Indeed, as discussed below,  ${}^8\text{Be}$  appears to have the intrinsic deformation of a  $2\alpha$  molecule. Higher in the spectrum is the famous pair of isospin-mixed  $(2^+; 0 + 1)$  states at 16.63 and 16.92 MeV which have widths of order 100 keV; the  $T = 1$  component is the isobaric analog of the  ${}^8\text{Li}$  ground state. There are similar  $(1^+; 0 + 1)$  and  $(3^+; 0 + 1)$  pairs near 18 and 19 MeV which have widths less than 300 keV. Many additional states have been identified above 18 MeV, most

of them with large widths, up to the  $(0^+; 2)$  isobaric analog of  ${}^8\text{He}$  at 27.49 MeV. There are also some negative-parity states in this region, which we have not attempted to calculate. In constructing  $\Psi_J$ , we use all p-shell states of symmetry [4] and [31], but neglect those of symmetry [22] and [211], as shown in Table IV.

The known experimental spectrum for  ${}^8\text{B}$  is similar to  ${}^8\text{Li}$ , except that with the extra Coulomb repulsion, the  $(2^+; 1)$  ground state is just barely strong stable, decaying by  $\beta+$  emission with a half life of 770 ms. The  $(1^+; 1)$  first excited state is seen as a narrow resonance in  ${}^7\text{Be}+p$  scattering, and the  $(3^+; 1)$  second excited state is much broader than its  ${}^8\text{Li}$  analog. The only other observed state is the  $(0^+; 2)$  isobaric analog to  ${}^8\text{He}$  at 10.62 MeV. The ground state for  ${}^8\text{C}$  is unstable against several possible breakup channels, having a width of  $\sim 230$  keV, but its mass excess is known within 20 keV. We have calculated the energies of these states in  ${}^8\text{B}$  and  ${}^8\text{C}$  so we can study the energy differences in the  $T = 1$  and 2 isomultiplets.

The full  $A = 8$  wave function is constructed by acting on the  $\Psi_J$ , Eq. (3.6), with the  $U_{ij}$ ,  $U_{ij}^{LS}$ ,  $U_{ijk}$ , and  $U_{ijk}^{TNI}$  correlations. Because of the tensor and other correlations in  $U_{ij}$ , many additional symmetry components, beyond the explicit p-shell states discussed above, are built up in the wave function. In principle, the  $U_{ij}$  could be generalized to be different according to whether particles  $i$  and  $j$  are in the s- or p-shell, but this would require a larger sum over the different partitions and would increase the computational cost by an order of magnitude.

For input to the GFMC algorithm, it is more efficient to use the somewhat simplified trial function

$$|\Psi_T\rangle = \mathcal{S} \prod_{i < j} \left( 1 + U_{ij} + \sum_{k \neq i, j} \tilde{U}_{ij;k}^{TNI} \right) |\Psi_J\rangle, \quad (3.14)$$

where  $\tilde{U}_{ij;k}^{TNI}$  is a truncated three-nucleon interaction correlation based on the short-range  $V_{ijk}^R$  term and on the anticommutator part of the two-pion exchange,  $V_{ij;k}^{2\pi,A}$ , which can be reduced to operators that depend only on the spins and isospins of nucleons  $i$  and  $j$ . Thus the sum over  $k$  can be made, leaving a two-body spin-isospin operator that can be combined with  $U_{ij}$ ; the result is calculable with only a little more effort than just  $U_{ij}$  alone. This trial function gets the bulk of the energy, as shown below, but for about half the computational effort of the full  $\Psi_V$ .

## B. Energy Evaluation

The energy expectation value of Eq. (3.1) is evaluated using Monte Carlo integration. A detailed technical description of the methods used here can be found in Refs. [10,15,16]. Monte Carlo sampling is done both in configuration space and in the discrete order of operators in the symmetrized product of the pair wave function by following a Metropolis random walk. The expectation value for an operator  $O$  with the full wave function  $\Psi_V$  is given by

$$\langle O \rangle = \frac{\sum_{p,q} \int d\mathbf{R} \left[ \Psi_{V,p}^\dagger(\mathbf{R}) O \Psi_{V,q}(\mathbf{R}) / W_{pq}(\mathbf{R}) \right] W_{pq}(\mathbf{R})}{\sum_{p,q} \int d\mathbf{R} \left[ \Psi_{V,p}^\dagger(\mathbf{R}) \Psi_{V,q}(\mathbf{R}) / W_{pq}(\mathbf{R}) \right] W_{pq}(\mathbf{R})}, \quad (3.15)$$

where we have introduced a probability distribution,  $W_{pq}(\mathbf{R})$ , based on the approximate wave function  $\Psi_P$  of Eq. (3.3),

$$W_{pq}(\mathbf{R}) = |\text{Re}(\langle \Psi_{P,p}^\dagger(\mathbf{R}) \Psi_{P,q}(\mathbf{R}) \rangle)| . \quad (3.16)$$

The subscripts  $p$  and  $q$  specify the order of operators on the left and right hand side of the pair wave functions, while the integration runs over the particle coordinates  $\mathbf{R} = (\mathbf{r}_1, \mathbf{r}_2, \dots, \mathbf{r}_A)$ . This probability distribution is much less expensive to compute than one using the full wave function of Eq. (3.2) with its spin-orbit and operator-dependent three-body correlations, but the denominator of Eq. (3.15) is typically within 1-2% of unity. Expectation values have a statistical error which can be estimated by the standard deviation  $\sigma$  in either gaussian approximation or by using block averaging schemes.

Our wave functions are vectors of  $2^A \times I(A, T)$  complex numbers,

$$\Psi(\mathbf{R}) = \sum_{\alpha} \psi_{\alpha}(\mathbf{R}) |\alpha\rangle , \quad (3.17)$$

where the  $\psi_{\alpha}(\mathbf{R})$  are the coefficients of each possible spin-isospin state  $|\alpha\rangle$  with specific third components of the spins of each nucleon and the desired total isospin. The CD and CSB force components are sufficiently small that we do not worry about isospin mixing in the wave function, and the expression for the number of isospin states,  $I(A, T)$ , is given in Ref. [1]. This gives arrays with 3584, 5120, and 7168 elements for  ${}^8\text{Be}$ ,  ${}^8\text{He}$ , and  ${}^8\text{Li}$ , respectively. The spin, isospin, and tensor operators  $O_{ij}^{p=2,6}$  contained in the two-body correlation operator  $U_{ij}$ , and in the Hamiltonian are sparse matrices in this basis.

Expectation values of the kinetic energy and spin-orbit potential require the computation of first derivatives and diagonal second derivatives of the wave function. These are obtained by evaluating the wave function at  $6A$  slightly shifted positions of the coordinates  $\mathbf{R}$  and taking finite differences, as discussed in Ref. [10]. Potential terms quadratic in  $\mathbf{L}$  require mixed second derivatives, which can be obtained by additional wave function evaluations and finite differences. A rotation trick can be used to reduce the number of additional locations at which the wave function must be evaluated [17].

In addition to calculating energies, we evaluate  $\langle J^2 \rangle$  and  $\langle J_z \rangle$  expectation values to verify that our wave functions truly have the specified quantum numbers. Another check is made on the antisymmetry of the Jastrow wave function by evaluating, at an initial randomized position,

$$\frac{\Psi_J^\dagger [1 + P_{ij}^x P_{ij}^\sigma P_{ij}^\tau] \Psi_J}{\Psi_J^\dagger \Psi_J} , \quad (3.18)$$

where  $P_{ij}^{x,\sigma,\tau}$  are the space, spin, and isospin exchange operators. This value should be exactly zero for an antisymmetric wave function, and it is in fact less than  $10^{-9}$  for each pair of particles in each nuclear state that we study.

A major problem arises in minimizing the variational energy for p-shell nuclei using the above wave functions: there is no variational minimum that gives reasonable rms radii. For example, the variational energy for  ${}^6\text{Li}$  is slightly more bound than for  ${}^4\text{He}$ , but is not more bound than for separated  ${}^4\text{He}$  and  ${}^2\text{H}$  nuclei, so the wave function is not stable against breakup into  $\alpha + d$  subclusters. Consequently, the energy can be lowered toward the sum

of  ${}^4\text{He}$  and  ${}^2\text{H}$  energies by making the wave function more and more diffuse. Such a diffuse wave function would not be useful for computing other nuclear properties, or as a starting point for the GFMC calculation.

On the basis of our work in  $A = 6\text{--}7$  nuclei, we believe that part of the problem is a fault of the Hamiltonian, but most of it is due to the presence of small admixtures of highly excited states in the trial function [1]. In that work, we constrained our search for optimal variational parameters by requiring the resulting point proton rms radius,  $r_p$ , to be close to the experimental values for  ${}^6\text{Li}$  and  ${}^7\text{Li}$  ground states. Then we allowed only small variations in the construction of the  ${}^6\text{He}$  and  ${}^7\text{Be}$  ground states and all the excited or resonant states, for which there are no experimental measurements of the charge radii.

In the present work, we have the additional complication that all the  $A = 8$  nuclei are sufficiently short-lived that precise experimental determinations of their radii exist do not exist. Consequently, the variational parameters in Table I are chosen very close to those of our previous work, with only a systematic reduction in the depth of the Woods-Saxon potential well as  $L$  increases, and an increase in the tail of the  $f_{pp}^{[n]}(r)$  correlation as the spatial symmetry declines, as shown in Table I. These gradual changes help to insure that the radii of excited states increase as the excitation energy increases.

The last step is always the diagonalization to determine the  $\beta_{LS[n]}$  mixing coefficients of Tables II-IV. Shell model lore tells us that the lowest state of any given  $(J^\pi; T)$  will be the state with maximal spatial symmetry and smallest  $L$  that can be formed from the allowed couplings, e.g., the  ${}^1\text{S}[4]$  ground state in  ${}^8\text{Be}$  or the  ${}^3\text{P}[31]$  ground state in  ${}^8\text{Li}$ . For the purposes of obtaining a variational upper bound and a GFMC starting point, we could settle for a  $\Psi_V$  constructed using only that  $LS[n]$  component. However, by using more components, we can gain a significant amount of energy in some cases and this gain persists in our GFMC propagations. For the  ${}^8\text{He}$  ground state, when the dominant  ${}^1\text{S}[22]$  piece is supplemented by the  ${}^3\text{P}[211]$  term, the energy gain is 1.2 MeV. In the case of  ${}^8\text{Li}$  ground state, where the dominant term is  ${}^3\text{P}[31]$ , addition of the three other contributing [31] symmetry states lowers the energy 0.8 MeV; addition of the one [22] state (the next highest spatial symmetry) gives only an additional 0.1 MeV. However, for the  ${}^8\text{Be}$  ground state, with the dominant  ${}^1\text{S}[4]$  term, addition of the one [31] symmetry piece gives only 0.1 MeV. For this reason, we feel reasonably confident in truncating the  ${}^8\text{Li}$  and  ${}^8\text{Be}$  p-shell bases after the top two symmetry states.

#### IV. GREEN'S FUNCTION MONTE CARLO

A detailed description of the nuclear GFMC method, and many tests of its accuracy, are given in Ref. [1]. In this section we present a brief review of the method and then describe two improvements that have been made since that publication. In most of this section, we will not make the distinction between  $H'$  and  $H$ ; the reader should remember that in fact we use the simpler  $H'$  in our GFMC propagator and evaluate  $\langle H - H' \rangle$  perturbatively.

## A. Review

The GFMC method starts with the trial wave function,  $\Psi_T$  of Eq. (3.14), and projects out of it the exact lowest energy state with the same quantum numbers,  $\Psi_0$ :

$$\Psi_0 = \lim_{\tau \rightarrow \infty} \Psi(\tau) , \quad (4.1)$$

$$\Psi(\tau) = e^{-(H-E_0)\tau} \Psi_T = \left[ e^{-(H-E_0)\Delta\tau} \right]^n \Psi_T . \quad (4.2)$$

Here we have sliced the imaginary propagation time,  $\tau$ , into a number of small time steps,  $\Delta\tau = \tau/n$ . The small-time-step Green's function,  $G_{\alpha\beta}(\mathbf{R}, \mathbf{R}')$ , is a matrix function of  $\mathbf{R}$  and  $\mathbf{R}'$  in spin-isospin space, with matrix elements defined as

$$G_{\alpha\beta}(\mathbf{R}, \mathbf{R}') = \langle \mathbf{R}, \alpha | e^{-(H-E_0)\Delta\tau} | \mathbf{R}', \beta \rangle . \quad (4.3)$$

Then  $\Psi(\mathbf{R}_n, \tau)$  is given by

$$\Psi(\mathbf{R}_n, \tau) = \int G(\mathbf{R}_n, \mathbf{R}_{n-1}) \cdots G(\mathbf{R}_1, \mathbf{R}_0) \Psi_T(\mathbf{R}_0) d\mathbf{R}_{n-1} \cdots d\mathbf{R}_1 d\mathbf{R}_0 . \quad (4.4)$$

The small-time-step propagator used in Ref. [1] is

$$\begin{aligned} G_{\alpha\beta}(\mathbf{R}, \mathbf{R}') &= e^{E_0\Delta\tau} G_0(\mathbf{R}, \mathbf{R}') \exp \left[ -\frac{\Delta\tau}{2} \sum (V_{ijk}^R(\mathbf{R}) + V_{ijk}^R(\mathbf{R}')) \right] \\ &\times \langle \alpha | I_3(\mathbf{R}) | \gamma \rangle \langle \gamma | \left[ \mathcal{S} \prod_{i < j} \frac{g_{ij}(\mathbf{r}_{ij}, \mathbf{r}'_{ij})}{g_{0,ij}(\mathbf{r}_{ij}, \mathbf{r}'_{ij})} \right] | \delta \rangle \langle \delta | I_3(\mathbf{R}') | \beta \rangle , \end{aligned} \quad (4.5)$$

where  $g_{ij}(\mathbf{r}_{ij}, \mathbf{r}'_{ij})$  is the exact two-body propagator,  $g_{0,ij}(\mathbf{r}_{ij}, \mathbf{r}'_{ij})$  is the free two-body propagator,  $G_0(\mathbf{R}, \mathbf{R}')$  is the free many-body propagator,  $\alpha, \beta, \gamma, \delta$  are spin-isospin state indices, and summation over  $\gamma, \delta$  is implied. There is also an implicit sampling of the order of pairs in the symmetrized product of Eq. (4.5). The construction of the exact two-body propagator is described in Ref. [1]. The influence of the three-nucleon potential on the many-body propagator is broken into two pieces: the scalar  $V_{ijk}^R$  which is easily exponentiated, and the  $V_{ijk}^{2\pi}$  which is a more complicated operator in spin-isospin space. The simplest treatment of this term in the TNI is to expand to first order in  $\Delta\tau$ ,

$$I_3(\mathbf{R}) = 1 - \frac{\Delta\tau}{2} \sum V_{ijk}^{2\pi}(\mathbf{R}) ; \quad (4.6)$$

in fact we use a more efficient procedure described below in subsection E.

The integrals in Eq. (4.4) are evaluated stochastically by averaging over a set of  $n$ -step paths,  $\mathbf{P}_n = \mathbf{R}_0, \mathbf{R}_1, \dots, \mathbf{R}_n$ . The paths are chosen by first sampling a set of positions,  $\mathbf{R}_0$ , using a probability function based on  $\Psi_T(\mathbf{R}_0)$ , and then sequentially sampling the free Green's functions,  $G_0(\mathbf{R}_{i+1}, \mathbf{R}_i)$ , to generate  $\mathbf{R}_{i+1}$  from  $\mathbf{R}_i$ . We thus obtain a spin-isospin vector  $\Psi(\mathbf{P}_n)$  which is one sample of the integrand of Eq. (4.4). A GFMC “configuration” consists of the position,  $\mathbf{R}_n$ , and the vector  $\Psi(\mathbf{P}_n)$ . Branching and importance sampling,

described in detail in Ref. [1], are used to obtain samples with probability proportional to the scalar importance function  $I$ :

$$I[\Psi(\mathbf{P}_n), \Psi_{T,p}(\mathbf{R}_n)] = |\text{Re}[\sum_{\alpha} \psi_{\alpha}(\mathbf{P}_n)^{\dagger} \psi_{T,p,\alpha}(\mathbf{R}_n)]| + \epsilon \sum_{\alpha} |[\psi_{\alpha}(\mathbf{P}_n)^{\dagger} \psi_{T,p,\alpha}(\mathbf{R}_n)]|, \quad (4.7)$$

where the sums run over the spin-isospin states  $\alpha$ , and  $\Psi_{T,p}$  is the trial wave function evaluated with a specific choice of pair operator orders  $p$ . Here  $\epsilon$  is a small constant ( $\approx 0.01$ ) that ensures a positive-definite importance function so that diffusion can take place across nodal surfaces.

The GFMC method allows one to compute “mixed” expectation values:

$$\langle O \rangle_{Mixed} = \frac{\langle \Psi_T | O | \Psi(\tau) \rangle}{\langle \Psi_T | \Psi(\tau) \rangle}, \quad (4.8)$$

$$= \frac{\int d\mathbf{R}_n \Psi_T^{\dagger}(\mathbf{R}_n) O \Psi(\mathbf{R}_n, \tau)}{\int d\mathbf{R}_n \Psi_T^{\dagger}(\mathbf{R}_n) \Psi(\mathbf{R}_n, \tau)}. \quad (4.9)$$

Because  $H$  commutes with the propagator,  $\langle H(\tau) \rangle_{Mixed}$  is an upper bound to  $E_0$  and approaches  $E_0$  from above. However expectation values of operators that do not commute with  $H$  are extrapolated using

$$\begin{aligned} \langle O(\tau) \rangle &= \frac{\langle \Psi(\tau) | O | \Psi(\tau) \rangle}{\langle \Psi(\tau) | \Psi(\tau) \rangle}, \\ &\approx \langle O(\tau) \rangle_{Mixed} + [\langle O(\tau) \rangle_{Mixed} - \langle O \rangle_T], \end{aligned} \quad (4.10)$$

where

$$\langle O \rangle_T = \frac{\langle \Psi_T | O | \Psi_T \rangle}{\langle \Psi_T | \Psi_T \rangle}. \quad (4.11)$$

In the following we address refinements which have been made to the GFMC algorithm since Ref. [1]. These refinements are important in order to make calculations of larger nuclei feasible.

## B. Constrained Path Algorithm

Diffusion or Green’s function Monte Carlo simulations of many-fermion systems generally suffer from the so-called “fermion-sign problem”. In essence this results from stochastically evaluating matrix elements of the form encountered in Eq. (4.9). The Monte Carlo techniques used to calculate the path integrals leading to  $\Psi(\mathbf{R}_n, \tau)$  involve only local properties, while antisymmetry is a global property. This leads to integrands in Eq. (4.9) that have oscillating signs at large  $\tau$ , which cause the statistical error to grow exponentially with imaginary time. The problem is not insurmountable for light systems, because the states are fairly well separated and one can propagate for a substantial imaginary time without having unacceptable statistical errors. However, the sign problem also grows exponentially with particle number, as the interchange of any pair of nucleons causes a change in sign for the matrix element.

The sign problem significantly limits the maximum  $\tau$  that we can use in the simulations; hence we invoke an approximate technique to deal with it. The approximation involves keeping only a subset of the paths in evaluating the integrals, and using the knowledge gained in the VMC calculations to choose the subset of paths. It is closely related to methods used previously in condensed matter and elsewhere; they generally go by the name of constrained-path techniques [18,19]. Some details of the algorithm, however, are special to the nuclear physics case.

The basic idea of the constrained-path method is to discard those configurations that, in future generations, will contribute only noise to expectation values. If we knew the exact ground state  $|\Psi_0\rangle$ , we could discard any configuration for which:

$$\Psi(\mathbf{P}_n)^\dagger \Psi_0(\mathbf{R}_n) = 0 , \quad (4.12)$$

where a sum over spin-isospin states is implied. The sum of these discarded configurations can be written as a state  $|\Psi_d\rangle$ , which obviously has zero overlap with the ground state

$$\langle \Psi_d | \Psi_0 \rangle = 0 . \quad (4.13)$$

The  $\Psi_d$  contains only excited states and should decay away as  $\tau \rightarrow \infty$ , thus discarding it is justified. However, in general the ground state  $\Psi_0$  is not known exactly and hence the constraint is imposed approximately using  $\Psi_T$  in the place of  $\Psi_0$ .

In Green's function or Auxiliary Field Monte Carlo (AFMC) [20–22], the overlap of the configuration with the trial state evolves smoothly with time. The change of the configurations  $\Psi(\mathbf{P}_n)$  per time step scales with  $\sqrt{\Delta\tau}$ , which can be made arbitrarily small. If the wave function of the system is a purely real scalar quantity, any configuration which yields a negative overlap must first pass through a point at which  $\Psi_T$  and hence the overlap is zero. Discarding configurations at this point is sufficient to stabilize the simulation and produce an approximate solution  $\Psi_C$  to the many-fermion problem. It solves the many-body Schrödinger equation with the boundary conditions imposed by the nodes of  $\Psi_T$ , and is known as the fixed-node approximation [23–26]. The approximate  $\Psi_C$  is the best wave function (in the sense of lowest energy) with the same nodes as  $\Psi_T$ . The discarded configurations are orthogonal not only to the trial state but also to the solution of the constrained problem  $\Psi_C$ , and it has been shown that this method produces an upper bound to the ground state energy [25].

More generally, and particularly in nuclei, the trial wave function  $\Psi_T$  is a vector in spin-isospin space, and there are no coordinates for which all the spin-isospin amplitudes are zero. This is also true in AFMC, where the propagated configurations describe a fully antisymmetric product of single-particle wave functions. In both these cases, the evolution of the wave function remains smooth. In AFMC it is still possible to use a constraint of the form given in Eq. (4.13). However, the discarded configurations, while orthogonal to the trial state  $\Psi_T$ , are not necessarily orthogonal to the the solution in the constrained space  $\Psi_C$ . For this reason, the method does not produce an upper bound to the true ground-state energy [27].

A new difficulty specific to the nuclear problem is that the overlap  $\Psi_{T,p}(\mathbf{R}_n)^\dagger \Psi(\mathbf{P}_n)$  is complex, and is estimated stochastically with a randomly selected order, denoted by the subscript  $p$ , of the operators in  $\Psi_T$ , Eq. (3.14). These overlaps do not evolve smoothly and

pass through zero. Therefore we can satisfy the constraint Eq. (4.13) only on the sum of discarded configurations ( $\Psi_d$ ), but not for individual configurations as in Eq. (4.12).

The fluctuations in  $\Psi_{T,p}$ , due to the sampling of the pair operator orders, are small compared to the wave function itself, so we define an algorithm for discarding configurations which resembles as much as possible the fixed-node or constrained-path algorithms described above. Configurations in the GFMC are obtained with probability proportional to the importance function  $I_{T,p} = I[\Psi(\mathbf{P}_n), \Psi_{T,p}]$ , Eq. (4.7), which depends upon  $p$ . For each of them the overlap  $O_{T,p}$  is defined as:

$$O_{T,p} = \text{Re}[\Psi(\mathbf{P}_n)^\dagger \Psi_{T,p}(\mathbf{R}_n)] , \quad (4.14)$$

so that the required constraint is the sum over discarded configurations of  $O_{T,p}/I_{T,p} = 0$ . We define a probability  $P[\Psi(\mathbf{P}_n), \Psi_{T,p}(\mathbf{R}_n)]$  for discarding a configuration in terms of the ratio  $O_{T,p}/I_{T,p}$ :

$$\begin{aligned} P[\Psi(\mathbf{P}_n), \Psi_{T,p}(\mathbf{R}_n)] &= 0 & O/I &> \alpha_c \\ &= \frac{\alpha_c - O/I}{\alpha_c - \beta_c} & \alpha_c &> O/I > \beta_c \\ &= 1 & O/I &< \beta_c . \end{aligned} \quad (4.15)$$

According to this algorithm configurations with  $O/I$  less than  $\beta_c$  are always discarded, configurations with  $O/I$  greater than  $\alpha_c$  are never discarded, and there is a linear interpolation in between. The values of  $\alpha_c$  and  $\beta_c$  are held constant during the simulation. At each step, a configuration is discarded with a probability that depends upon the order of pair operators  $p$ . Hence an unbiased estimate of the overlap  $\langle \Psi_d | \Psi_T \rangle$  is required. It is obtained by choosing independent samples  $p'$  of the pair operator order to compute the overlap:

$$\langle \Psi_d | \Psi_T \rangle = \sum_{\substack{\text{discarded} \\ \text{configurations}}} O_{T,p'}/I_{T,p'} . \quad (4.16)$$

One or two preliminary runs are sufficient to adjust the constants  $\alpha_c$  and  $\beta_c$  such that this overlap is zero within statistical errors. When this condition is satisfied, it is trivial to show that the growth estimate of the energy, obtained from the growth or decay of the population with imaginary time, is identical to the mixed estimate. These two energy estimators are described in detail in Ref. [1].

Note that in absence of the term with  $\epsilon$  in the importance function  $I_{T,p}$ , Eq. (4.7), the ratio  $O_{T,p}/I_{T,p}$  is  $\pm 1$ . In constrained path calculations, a significantly larger value of  $\epsilon$ , typically 0.15, is used to reduce the fluctuations in  $O_{T,p}/I_{T,p}$ . For light nuclei, we have tried a variety of  $\alpha_c$  and  $\beta_c$  adjusted to the constraint without finding any statistically significant differences in the results. Indeed, even preliminary estimates of  $\alpha_c$  and  $\beta_c$  which do not precisely satisfy the constraint condition Eq. (4.13) yield results indistinguishable from the results with finely tuned constraint parameters. Typical values of  $\alpha_c$  and  $\beta_c$  for  $A = 8$  are 0.1 and 0.2 respectively.

In principle, two parameters are not needed to adjust the constraint to yield zero overlap. We were motivated to try this approach by the fact that, in standard fixed-node calculations, one defines a propagator which goes exactly to zero at the node. This results in some configurations being discarded which have small positive overlaps, as well as all configurations

which have negative overlaps. In the fixed node scheme, this produces a result of higher order in the time step than simply discarding configurations with negative overlaps. For this reason both  $\alpha_c$  and  $\beta_c$  are chosen to be greater than zero. The algorithm described above is related to one proposed by Sorella in the context of condensed matter simulations [28], but simpler in that it uses only the overlap and the constraint parameters are held fixed during the simulation.

As discussed in the next subsection this method yields results with stable statistical errors independent of  $\tau$ . For  $A \leq 7$ , the calculated energy is very close to that obtained without constraints in most cases; however in some cases, particularly those with poor  $\Psi_T$ 's, the calculated energy can be significantly below or above the true unconstrained result. The amplitudes of the excited states  $\Psi_i$ , with energies  $E_i$ , in  $\Psi_T$  decay exponentially as  $\exp(-(E_i - E_0)\tau)$  in the unconstrained  $\Psi(\tau)$  without any change in their phase. Therefore these give a positive contribution to the mixed energy, making it  $\geq E_0$ . The equality is obtained in the limit  $\tau \rightarrow 0$ . The constrained energy can have additional errors if, due to a poor choice of  $\Psi_T$ , high-energy excitations get reintroduced in  $\Psi(\tau) - \Psi_d$ . Such excitations do not necessarily have the same phase as in  $\Psi_T$  and can give contributions to the constrained  $E(\tau)$  of either sign. Such errors can be easily detected by propagating  $\Psi(\tau) - \Psi_d$  without constraint for a limited number of steps  $n_u$ . Most of the  $\Psi_T$  dependence of the calculated energy is eliminated by fairly small  $n_u$  without a significant increase in the statistical error. Thus the wave function  $\Psi_C(\tau, n_u)$  used to estimate energies and other observables in the present calculations, is obtained from:

$$\Psi_C(\tau = n\Delta\tau, n_u) = \{\exp[-Hn_u\Delta\tau]\}_u \{\exp[-H(n - n_u)\Delta\tau]\}_c \Psi_T , \quad (4.17)$$

where  $\{\dots\}_c$  signifies propagation with the constraint and  $\{\dots\}_u$  indicates normal propagation without constraints. As is shown in the next subsection, the simulations are stable for arbitrary  $n$ , and a fairly small  $n_u$  ( $n_u\Delta\tau \leq 0.01$  MeV $^{-1}$ ) is sufficient to eliminate the  $\Psi_T$  dependence. Evaluation of matrix elements of this wave function can be implemented very easily on the computer by, after each propagation step, labeling those configurations which are to be discarded and then retaining them in the simulation for  $n_u$  more steps. In principle this could be used to evaluate the overlap of the discarded configurations with  $\Psi_T$  after the unconstrained propagation. This could result in better values of the constraint parameters, however we find no change in the overlap for the values of  $n_u$  we have considered.

### C. Tests of Constrained Path

We have tested the constrained path algorithm in a variety of light nuclear systems, studying the dependence upon constraining wave function and also the convergence of the results obtained by relaxing the constraint. In some cases bad trial wave functions were used to test the algorithm under extreme conditions. In this subsection we present results for the  ${}^6\text{Li}$  and  ${}^8\text{He}$  ground states and for 8 neutrons bound in an external well. The tests for  ${}^6\text{Li}$  and 8 neutrons were made using  $H = H'$ , Eq. (2.11), with no three-body potential. This eliminates uncertainties from the extrapolation of  $H - H'$ , and allows us to have just the exact two-body propagator,  $g_{ij}$ . Eliminating the three-body potential also results in faster calculations allowing smaller statistical errors to be achieved. In the following all energies

are in MeV and imaginary times in MeV<sup>-1</sup>; for simplicity the units are omitted in most cases.

Figure 2 shows the ground state energy of  ${}^6\text{Li}$  calculated with two choices of  $\Psi_T$  [Eq. (3.14)]: (1)  $\Psi_t$ , which is the full wave function with no  $\tilde{U}_{ij;k}^{TNI}$  because there is no  $V_{ijk}$ , and (2)  $\Psi_\sigma$ , a simplified wave function obtained by removing the tensor pair correlations leaving only spin-spin and isospin correlations. The subscript  $t$  on  $\Psi_t$  emphasizes that it has the essential tensor correlations. In this and the following two figures, constrained-propagation results with zero and finite  $n_u$  are shown as open symbols while solid symbols show completely unconstrained results or unconstrained continuations of constrained propagations. Averages of the last few energies are shown by solid lines with the corresponding statistical errors indicated by the surrounding dashed lines; the length of the line indicates the range of  $\tau$  included in the average. Consider first the results using the full ( $\Psi_t$ ) wave function shown in the upper part of Fig. 2; these are typical of our production calculations. The solid circles show an unconstrained propagation from  $\tau = 0$  to  $\tau = 0.1$  of 200,000 configurations; the statistical errors on the last points are growing rapidly, but the energy seems to be fairly independent of  $\tau$  beyond 0.05. The average from  $\tau = 0.06$  to  $\tau = 0.1$  is  $-28.16(12)$ , as shown by horizontal solid and dashed lines. It should be close to the correct answer for this Hamiltonian. The open triangles show constrained results with  $n_u = 0$  for the same case. This simulation is stable with much smaller statistical errors than the unconstrained calculation and could be extended to an arbitrarily large  $\tau$ ; here we find no significant change after  $\tau = 0.05$ . The average over  $0.14 \leq \tau \leq 0.20$  is  $-27.94(2)$ . We released the constraint at  $\tau = 0.20$  and continued the propagation to  $\tau = 0.27$ , as shown by solid triangles. The errors grow, and the average over this entire region is  $-28.15(5)$ . It is likely that this result, which is consistent with the unconstrained result of  $-28.16(12)$  but with smaller statistical error, is the most accurate available. A constrained propagation with  $n_u = 20$  is shown by the open squares; only 50,000 configurations were used. This simulation is very similar to the  $n_u = 0$  one; the average is  $-28.01(5)$ . These results suggest that constrained propagation with our typical  $\Psi_t$ , using  $n_u = 20$ , may lead to an error of  $+0.14(7)$  (or  $\sim 0.5\%$ ) in the binding energy of  ${}^6\text{Li}$ .

The results in the lower part of Fig. 2 were obtained using the  $\Psi_\sigma$  trial wave function. This is an extremely bad  $\Psi_T$  because, with no tensor correlations, this wave function results in an identically zero expectation value for the tensor potentials. Thus while the  $\tau = 0.0$  expectation value for  $\Psi_t$  is  $-23.95(4)$ , that for  $\Psi_\sigma$  is  $+31.1(1)$ . The solid circles show an unconstrained propagation of 400,000 configurations for this  $\Psi_\sigma$  case; the GFMC has managed to improve the  $\tau = 0.0$  energy by 59 MeV to  $-28.0(2)$ , but the statistical errors are large even after using twice the number of configurations as for the unconstrained propagation with  $\Psi_t$ . The open triangles show  $n_u = 0$  constrained propagation of 200,000 configurations. This propagation becomes stable after  $\tau = 0.12$ , but it has converged to the significantly overbound result of  $-30.2(1)$ . The solid triangles show the results of releasing the constraint at  $\tau = 0.20$ ; the energy immediately goes up to the correct value with an average of  $-28.0(2)$ . Finally the open squares show  $n_u = 20$  constrained propagation of 400,000 configurations. The repeated use of 20 unconstrained steps gives a stable propagation that is quite accurate; the average is  $-28.27(7)$  with an error of  $-0.12(9)$ . The unconstrained continuation of this calculation, shown by the solid squares, makes no significant change. These results show the need to have unconstrained steps before evaluation of the energy or any other observable.

The second test case is a system of 8 neutrons bound in an external one-body potential. We have previously reported results for such systems as a basis for comparing Skyrme models with microscopic calculations based on realistic interactions [29]. As in the previous example, the neutrons interact via the  $v'_{ij}$ , with no three-nucleon interaction. Because systems of neutrons are not self binding, the Hamiltonian also includes an external one-body potential of Woods-Saxon form,

$$V_1(r) = \sum_i \frac{V_0}{1 + \exp[-(r_i - r_0)/a_0]} ; \quad (4.18)$$

the parameters are  $V_0 = -20$  MeV,  $r_0 = 3.0$  fm, and  $a_0 = 0.65$  fm. Neither the external well nor the internal  $v'_{ij}$  potential are individually attractive enough to produce a bound state of eight neutrons, however the combination does produce binding.

The Jastrow  $\Psi_J$  for neutron drops is just

$$|\Psi_J\rangle = \prod_{i < j} f_c(r_{ij}) |\Phi_A(JM)\rangle . \quad (4.19)$$

where  $\Phi_A$  is a Slater determinant of single-particle orbitals. We compare results obtained with the full  $\Psi_T$ , again referred to as  $\Psi_t$  because of the tensor operators, shown in the upper part of Fig. 3, with those obtained with the  $\Psi_J$ , shown in the lower part.

The solid circles show results of unconstrained propagation using 400,000 configurations of the  $\Psi_t$  and 560,000 configurations of the  $\Psi_J$  trial wave functions, respectively. The errors are growing rapidly by  $\tau = 0.06$ , and the calculations do not appear to have converged. Averages of the last four energies are  $-39.3(1)$  and  $-38.9(1)$  for  $\Psi_t$  and  $\Psi_J$  respectively, but these are clearly just upper bounds. Constrained propagations using the  $\Psi_J$  trial wave function and  $n_u = 0$  and  $n_u = 20$  are shown by the open triangles and squares, respectively in the lower part of the figure. These have stabilized beyond  $\tau = 0.1$ , with end averages of respectively  $-39.58(4)$  and  $-39.79(6)$ . Both propagations were continued without constraint; their results are shown by solid triangles and squares. The energy remains stable but the errors grow rapidly; the averages are  $-39.86(11)$  and  $-39.85(34)$ . In this case constrained propagation with  $n_u = 20$  gives results that are below the best unconstrained (starting from  $\tau = 0$ ) upper bound with  $\Psi_t$  by  $0.5(1)$ . The constrained result is consistent with unconstrained continuations beyond  $\tau = 0.25$ , indicating its reliability.

A different situation obtains with the variationally better  $\Psi_t$  trial wave function; the  $\tau = 0$ , VMC energy for  $\Psi_t$ ,  $-35.30(4)$ , is lower than the  $-30.62(9)$  given by  $\Psi_J$ , but the difference is not as large as in the case of  ${}^6\text{Li}$ . Constrained propagation using  $\Psi_t$  and  $n_u = 0$  is shown by the open triangles in the upper part; it stabilizes beyond  $\tau = 0.1$ , but at a value that is 1 MeV too high. The results of releasing the constraint are shown by the solid triangles; the energy immediately drops 1 MeV and the final average is  $-39.71(10)$ . Finally constrained propagation for  $\Psi_t$  and  $n_u = 20$  is shown by the open squares. The results are stable with an average of  $-39.74(5)$ , in agreement with the best results obtained in the previous paragraph. Releasing the constraint does not result in any significant change, as is shown by the solid squares. This case also confirms the need to release the constraint before measurements, with the surprising result that a variationally better wave function may not necessarily provide better constraints to guide the GFMC. Nevertheless, constrained propagation with  $n_u = 20$  gives results with presumably less than 1% error, for both trial wave functions.

Finally, in Fig. 4 we show results for the  ${}^8\text{He}$  ground state with the full Argonne  $v_{18}$  plus Urbana IX three-nucleon interaction. We are presenting this case because we find that  ${}^8\text{He}$  is the most difficult nucleus we have studied, in terms of obtaining reliable error estimates, and the need for  $n_u > 0$ . All of the calculations are made with the full  $\Psi_T$  of Eq. (3.14). In this figure the results of a standard calculation without constraint (solid circles) are compared to those with constrained-path  $n_u = 0$  (open triangles) and  $n_u = 20$  (open squares), and their unconstrained continuation beyond  $\tau = 0.2$  shown by solid triangles and squares. The average unconstrained energy in the  $0.03 \leq \tau \leq 0.06$  range,  $-26.1(3)$ , is clearly an unconverged upper bound. The  $n_u = 0$  and 20 end averages,  $-26.89(9)$  and  $-27.16(15)$ , are below it by  $\sim 1$  MeV. The averages of the results obtained after the constraint is released at  $\tau = 0.2$ ,  $-27.5(4)$  and  $-26.9(2)$ , are not significantly different from the constrained averages.

From these, and many other, tests we conclude that constrained propagation, including unconstrained steps prior to measurement, yields results that are reliable. In the  $A = 8$  nuclei and neutron drops they are up to 4% below the unconverged upper bounds that can be obtained by unconstrained propagation up to  $\tau = 0.06$ , and have smaller statistical errors. The constrained path results with  $n_u \sim 10$  to 20 are stable within 1% with respect to reasonable, and in case of  ${}^6\text{Li}$  even unreasonable, changes in  $\Psi_T$  used to constrain the paths. Our present practice is to use the full  $\Psi_T$ , Eq. (3.14) in constrained path calculations with  $n_u = 20$  for the neutron-rich He isotopes and neutron drops and  $n_u = 10$  for all other nuclei where even  $n_u = 0$  calculations seem to be fairly accurate.

#### D. Resonance states in constrained-path algorithms

Since the constrained-path algorithm is stable to large imaginary time, it is useful to consider the large- $\tau$  behavior of the energy of resonant states. The bound-state simulations described above yield asymptotically stable energies out to very large imaginary times. Resonant states, however, are more delicate. In principle these states should decay to separated clusters, and in fact this does occur with the constrained-path algorithm. The rate of this decay presumably depends not only on the resonance energy but also on the width of the state, and the trial state wave function used to impose the constraint.

We have studied several cases including the two unbound p-wave states in  ${}^5\text{He}$ . The GFMC energy consistently decreases with  $\tau$  for both the  $J^\pi = 1/2^-$  and the  $3/2^-$  states. The  $1/2^-$  state, lying higher in energy and with a larger width, decays more quickly than the  $3/2^-$  state. We have verified that the system breaks apart into a separated  $\alpha$  plus  $n$  by studying the  $pp$  pair distribution function, which depends only upon the internal structure of the  $\alpha$ -particle. This distribution remains constant out to the largest imaginary times (3 MeV $^{-1}$ ) studied, while the  $pn$  and  $nn$  distributions steadily become broader.

We have also studied three low-lying states in  ${}^6\text{Li}$  out to large  $\tau$ . The  $J^\pi = 1^+$  ground state is stable, the  $3^+$  excitation is a narrow resonance, while the  $2^+$  state lies higher in energy and is broader. The GFMC energies of these states are displayed in Fig. 5 as a function of  $\tau$ . The ground state is clearly stable out to the largest imaginary times. The narrow  $3^+$  shows a plateau in  $E(\tau)$ , decreasing only modestly in energy, though of course it will eventually also decay to the  $\alpha+d$  threshold energy. The  $2^+$  state is much broader and decays much more quickly in imaginary time. Therefore, comparison of the energies obtained for such broad states with experiment could be misleading. The  $\alpha+d$  threshold

energy for this Hamiltonian is shown in the figure; it is clear that both excited states are far from convergence to this energy.

It is possible to compute energies that may be directly compared with experiment for resonant states that have only a single two-body channel available for breakup [30]. Scattering observables, including scattering length, effective range, and phase shifts, can be calculated directly by imposing scattering boundary conditions on the asymptotic wave function. This is quite important for studying a variety of interesting low energy reactions, including parity-violation and important astrophysical reactions, but has not been considered in this work.

### E. Three-body Propagator

The small-time-step propagator of Eq. (4.5) involves two complete evaluations of the three-body potential (two sums over all triples) and one product of all pair propagators for each time step. Thus as the number of nucleons is increased, the time spent in the three-body part of the propagation becomes a larger and larger fraction of the total time for the calculation. For this reason it is desirable to find a less costly treatment of the three-body propagator.

It was noted in Eq. (3.14) that the full  $U_{ijk}^{TNI}$  can be replaced with a  $\tilde{U}_{ijk}^{TNI}$  that omits the commutator part of  $V_{ijk}^{2\pi}$  with very little degradation of the variational energy, and that the resulting correlation is an operator in the spins and isospins of only two nucleons. This led us to consider the combined two- and three-body propagator (we omit the spin-isospin indices):

$$\tilde{G}(\mathbf{R}, \mathbf{R}') = e^{E_o \Delta \tau} \mathcal{S} \prod_{i < j} \frac{\tilde{g}_{ij}(\mathbf{r}_{ij}, \mathbf{r}'_{ij})}{g_{0,ij}(\mathbf{r}_{ij}, \mathbf{r}'_{ij})} \quad (4.20)$$

$$\begin{aligned} \tilde{g}_{ij}(\mathbf{r}_{ij}, \mathbf{r}'_{ij}) &= \left[ 1 - \frac{\Delta \tau}{2} \sum_{k \neq i,j} \alpha V_{ij;k}^{2\pi,A}(\mathbf{R}) \right] g_{ij}(\mathbf{r}_{ij}, \mathbf{r}'_{ij}) \left[ 1 - \frac{\Delta \tau}{2} \sum_{k \neq i,j} \alpha V_{ij;k}^{2\pi,A}(\mathbf{R}') \right] \\ &\times \exp \left[ -\frac{\Delta \tau}{2} \sum_{k \neq i,j} (V_{ijk}^R(\mathbf{R}) + V_{ijk}^R(\mathbf{R}')) \right]. \end{aligned} \quad (4.21)$$

The  $V_{ij;k}^{2\pi,A}$  is defined in Eq. (2.9) as the anticommutator part of  $V_{ijk}^{2\pi}$ , and  $\alpha$  is chosen so that

$$\alpha \langle V^{2\pi,A} \rangle = \langle V^{2\pi} \rangle; \quad (4.22)$$

typically  $\alpha = 1.6$ . This  $\tilde{g}_{ij}$  can be reduced to a single  $4 \times 4$  operator in  $i, j$  spin space for each of the two isospin states, and thus takes little more time to evaluate than just  $g_{ij}$ . Propagation with just  $\tilde{G}$  gives much the same results as with the much more costly propagator of Eq. (4.5), but we attempt to make a more reliable propagation by using the following sequence as the basic propagation step:

$$\begin{aligned} &\tilde{G}(\mathbf{R}_{i+n}, \mathbf{R}_{i+n-1}) \tilde{G}(\mathbf{R}_{i+n-1}, \mathbf{R}_{i+n-2}) \cdots \tilde{G}(\mathbf{R}_{i+n/2+1}, \mathbf{R}_{i+n/2}) \\ &\times \{1 - n \Delta \tau \sum_{i < j < k} [V_{ijk}^{2\pi}(\mathbf{R}_{i+n/2}) - \alpha V_{ij;k}^{2\pi,A}(\mathbf{R}_{i+n/2})]\} \\ &\times \tilde{G}(\mathbf{R}_{i+n/2}, \mathbf{R}_{i+n/2-1}) \cdots \tilde{G}(\mathbf{R}_{i+1}, \mathbf{R}_i), \end{aligned} \quad (4.23)$$

where  $n$  is a small (typically 4) number of steps. Here we go from  $\mathbf{R}_i$  to  $\mathbf{R}_{i+n}$  by making  $n/2$  steps with  $\tilde{G}$ ; then applying  $n$  times the correction due to the difference of the complete  $V^{2\pi}$  and the approximate  $\alpha V^{2\pi,A}$ , both computed at the position  $\mathbf{R}_{i+n/2}$ ; and finally making another  $n/2$  steps to  $\mathbf{R}_{i+n}$ .

Table V shows the reliability of this method for  ${}^6\text{Li}(\text{gs})$ . The first line gives results with the old method, Eq. (4.5), and the next three lines use the new method with increasing values of  $n$  [ $n = \infty$  means that no correction for the approximation in  $\tilde{G}$  is made with Eq. (4.23)]. The last line shows results using just a two-body propagator; that is, the three-body potential is included only perturbatively. Clearly a three-body propagator is essential for obtaining results with  $< 1\%$  error, however the  $\tilde{G}$  is reliable to better than 1%.

## F. Numerical Evaluations

The p-shell GFMC calculations reported here were made with constrained-path propagation to  $\tau = 0.2 \text{ MeV}^{-1}$  using 400 steps of  $\Delta\tau = 0.0005 \text{ MeV}^{-1}$ . Energies and other observables were evaluated every 20 steps and the last 7 ( $\tau \geq 0.14 \text{ MeV}^{-1}$ ) values were averaged. At least 10 unconstrained steps were taken before the observables were computed (20 steps were used for  ${}^8\text{He}$ ). The  $A = 8$  results used 10,000 to 20,000 initial configurations. Once the propagation has stabilized (typically by  $\tau = 0.1 \text{ MeV}^{-1}$ ), the constraint removes from 0.7% [for  ${}^8\text{Be}(\text{gs})$ ] to 1.7% [for  ${}^8\text{Be}(3^+)$ ] of the configurations at each propagation step (the percentages for  ${}^8\text{He}$  and  ${}^8\text{Li}$  are in this range). The removed configurations are replaced by new ones generated by branching with the average branching probability chosen to maintain an approximately constant population.

Most of the GFMC calculations reported here were made on the 128-node SGI Origin 2000 in the Mathematics and Computer Science division of Argonne National Laboratory. The individual nodes in this machine are 250 MHz R10000 processors which (when the processors are not being shared with other users and memory remains local to each processor) deliver sustained speeds of  $\geq 200 \text{ MFLOPS}$  for the 8-nucleon calculations. This results in a 10,000 configuration calculation for  ${}^8\text{Be}$  taking about 460 node-hours. The approximate times required for other nuclei can be determined from Table VI. The columns of this table show the number of nucleons, the number of pairs, and the size of the spin-isospin vector. We find that the total calculational time is proportional to the product of these three numbers; this product (scaled to 1 for  ${}^8\text{Be}$ ) is given in the last column.

Typically we have computed the  $M = J$  state of a given nucleus; this allows us to directly evaluate the spectroscopic quadrupole moment and magnetic moment. Recently we have realized that if we compute the  $M = 0$  state of even- $A$  nuclei, the size of the spin-isospin vector can be reduced by a factor of two. This is done by observing that for even  $A$ ,

$$\Psi_{-s_1, -s_2, \dots, -s_A}(J, M=0) = (-1)^{\frac{1}{2}A+J-M_S} \Psi_{s_1, s_2, \dots, s_A}^*(J, M=0), \quad (4.24)$$

where  $s_i$  is the spin-projection of nucleon  $i$  and  $M_S = \sum s_i$ . Thus only half of the spin-isospin vector needs to be computed and stored, resulting in a saving of half the computer time for even  $A \geq 8$  nuclei. This saving is not included in the times discussed in the previous paragraph. Unfortunately, the corresponding relation in odd- $A$  nuclei relates  $\Psi_{-s_i}(J, M)$  to  $\Psi_{s_i}(J, -M)$  and thus does not reduce the computational effort.

## V. ENERGY RESULTS

### A. Ground-State and Excitation Energies

In this Section we present VMC and GFMC results for the Hamiltonian consisting of Argonne  $v_{18}$  plus Urbana IX. Figure 6 shows the  $E(\tau)$  for the lowest  $T = 0$ ,  $J^\pi = 0^+, 2^+, 4^+, 1^+, 3^+$  states of  ${}^8\text{Be}$ . The solid and dashed lines show the average energy and its statistical error; these numbers are reported in Tables VII and VIII. The  $E(\tau)$  are

$$E(\tau) = \langle H'(\tau) \rangle_{Mixed} + \langle H(\tau) - H'(\tau) \rangle, \quad (5.1)$$

where the  $\langle H - H' \rangle$  is perturbatively extrapolated by Eq. (4.10). Figures 7 and 8 show the corresponding  ${}^8\text{Li}$  and  ${}^8\text{He}$  results. In all cases for which the states are experimentally narrow or stable, the  $E(\tau)$  rapidly decreases for small  $\tau$  and stabilizes before  $\tau = 0.1 \text{ MeV}^{-1}$ . It is clear that  $E(\tau)$  has not converged by  $\tau = 0.2 \text{ MeV}^{-1}$  for the experimentally very broad  ${}^8\text{Be}(4^+)$  state, making it not possible to determine an accurate excitation energy for this state. The other broad states [ ${}^8\text{Be}(2^+)$  and  ${}^8\text{He}(2^+)$ ], and the experimentally unknown  ${}^8\text{He}(1^+)$  state seem reasonably converged.

Table VII shows the computed and experimental ground-state energies. The errors shown in parentheses are only the Monte Carlo statistical errors; the systematic errors discussed in the previous section and in Ref. [1] could add an additional 1% to the GFMC error. This paper is our first formal publication of  $A = 8$  results. Results for  $A = 6$  and 7 were published in Ref. [1]; most of the corresponding values in Table VII have been recomputed using improved VMC wave functions and GFMC propagation. Most of the VMC values have not changed significantly from those in Ref. [1]; the exception is  ${}^7\text{He}$  which is now constrained to what we think is a more reasonable rms radius and actually has a higher energy. The  $A = 6$  and 7 GFMC energies have now all been computed with constrained propagation to  $\tau = 0.2 \text{ MeV}^{-1}$  instead of the unconstrained propagation to only  $\tau = 0.06 \text{ MeV}^{-1}$  used in Ref. [1]. This has resulted in a lowering of  ${}^{6,7}\text{He}$  energies by 0.47(17) and 0.63(23) MeV respectively; other energies changed by less than 1%. For  $A = 8$  nuclei, the GFMC improves the  $\Psi_T$  energy by  $\sim 10$  MeV; our best  $\Psi_V$  provides only  $\sim 1.5$  MeV of this improvement.

Table VIII shows excitation energies for the  $A = 8$  nuclei. The errors are the combined statistical errors of the energies computed for the given state and the ground state. We see that, while the absolute VMC energies have substantial errors as compared to the GFMC values, the VMC excitation energies are typically within an MeV of the GFMC values.

Figure 9 shows the energies of nuclear states for  $4 \leq A \leq 8$  and Fig. 10 shows the corresponding excitation spectra. As is the case for the ground-state values, most of the  $A = 6$  and 7 excited-state energies have been recomputed with improved VMC wave functions and all of the GFMC propagations have been made to  $\tau = 0.2 \text{ MeV}^{-1}$ . The VMC excitation energies of the lowest  ${}^7\text{Li}(\frac{1}{2}^-)$  and  ${}^7\text{Li}(\frac{5}{2}^-)$  states have been significantly reduced from the values reported in Ref. [1]. These are the result of improved mixings of the different symmetry states in the variational wave function.

The figures confirm the principal  $A = 6$  and 7 results of Ref. [1] for  $A = 8$ : the Hamiltonian consisting of Argonne  $v_{18}$  plus Urbana IX underbinds nuclei in the p-shell with the underbinding becoming worse as one increases  $A$  or  $N - Z$ . However the predictions of the

excitation spectra are generally reasonable; the rms error of all of the 16 excitation energies computed by GFMC is only 650 keV; for the 9 states with experimental width less than 200 keV it is 540 keV. Considering that no parameters were adjusted to fit these p-shell energies, this is quite respectable. We do note that, where there is an experimental value to compare to, the VMC excitation energies of second excited states of a given  $J^\pi$ , which are very difficult to compute by GFMC, are usually too high.

Although the Argonne  $v_{18}$  plus Urbana IX Hamiltonian consistently underbinds the p-shell nuclei, the errors are small compared to the magnitudes of the potential energies. Table IX shows the perturbatively extrapolated GFMC expectation values for the kinetic energy and potential energy terms. As is discussed in Ref. [1], the perturbatively extrapolated GFMC terms do not add up to the total energy, which is the most reliable number computed by this method. The total two-body potential,  $v_{ij}$  is dominated by the one-pion exchange term,  $v_{ij}^\pi$ . There is a large cancellation between the kinetic and two-body potential energies so that their sum is only 15% to 20% of the two-body potential. The total three-body potential is typically 4% to 5% of the two-body potential. The repulsive  $V_{ijk}^R$  typically cancels 45% of the  $V_{ijk}^{2\pi}$ . As an indication of the smallness of the errors produced by this Hamiltonian, consider the ground state of  ${}^8\text{Be}$ : the difference of the computed and experimental energies is 2.1 MeV; the two-body potential is  $-301$  MeV,  $V_{ijk}^{2\pi} = -27$  MeV, and  $V_{ijk}^R = +12.3$  MeV. Thus the corrections that have to be made to  $V_{ijk}$  are significantly smaller than the terms already included.

## B. Isobaric Analog States

Energy differences of isobaric analog states are sensitive probes of the charge-independence-breaking parts of the Hamiltonian. To study these it is useful to express the energies in an isobaric multiplet, characterized by  $A$  and  $T$ , in terms of the isospin multipole operators of order  $n$ :

$$E_{A,T}(T_z) = \sum_{n \leq 2T} a_{A,T}^{(n)} Q_n(T, T_z) . \quad (5.2)$$

The  $Q_n(T, T_z)$  are orthogonal functions for projecting out isovector, isotensor, and higher-order terms [31]; the first terms are  $Q_0 = 1$ ,  $Q_1 = T_z$ , and  $Q_2 = \frac{1}{2}[3T_z^2 - T(T+1)]$ . The coefficients  $a^{(n)}$  are then obtained from the calculated energies:

$$a_{A,T}^{(n)} = \sum_{T_z} Q_n(T, T_z) E_{A,T}(T_z) / \sum_{T_z} Q_n^2(T, T_z) , \quad (5.3)$$

or perturbatively from expectation values of the isomultipole operators present in the Hamiltonian.

In first-order perturbation theory, the electromagnetic interaction contributes to the  $a^{(n)}$  for  $n = 0, 1$ , and  $2$ , the kinetic energy to  $n = 0$  and  $1$ , the nuclear CSB potential to  $n = 1$ , and the nuclear CD potential to  $n = 2$ . Because a significant portion of the  $v_{ij}^{CD}$  comes from one-pion exchange, there should also be a CD component to  $V_{ijk}^{2\pi}$ ; however, a plausible extension of the Urbana IX model gives negligible contributions of 3 keV or less to the  $n = 2$  terms. The  $a^{(n)}$  for higher  $n$  are zero in first order with our Hamiltonian, and there is little experimental evidence for  $n \geq 3$  terms in nuclei [32]. We have made VMC

calculations of the  $a^{(1)}$  and  $a^{(2)}$  in first order by using a CI wave function of good isospin,  $T$ , and simply varying  $T_z$  to compute the  $E_{A,T}(T_z)$ ; in the GFMC calculations we evaluate expectations of the isomultiplet operators for the  $T_z = -T$  nuclei. The CSB and CD parts of the Hamiltonian can induce corresponding changes in the nuclear wave functions, leading to higher-order perturbative corrections to the splitting of isospin mass multiplets. However, it is difficult for us to estimate these higher order effects reliably in either the VMC or GFMC calculations.

Table X shows results for the  $T = 1$  and  $2$  isovector and isotensor coefficients in  $A = 8$  nuclei compared to experiment. In obtaining the experimental  $a_{8,1}^{(2)}$  coefficient, we have used the average of the two isospin-mixed  $(2^+;0+1)$  states; our calculation of this mixing is discussed in the next subsection. The contributions of the complete  $v^\gamma$ ,  $v^{CD}$ ,  $v^{CSB}$ , and  $K^{CSB}$  terms to the  $a^{(n)}$  are also given. The results show that the present Hamiltonian and VMC wave function match the experimental CSB and CD of the  $T = 1$  multiplet fairly well, but the calculated value for  $a_{8,2}^{(1)}$  is about 10% too small. The GFMC consistently reduces the coefficients, mostly by reducing the Coulomb term. For the isovector coefficients, this worsens the comparison with experiment, however the case of  $a_{8,2}^{(2)}$  is significantly improved. In all these calculations, the Coulomb interaction between protons is the dominant contribution to the  $a^{(n)}$ , but the strong interaction CSB terms serve to bring the final results closer to experiment. However, in view of the fact that the  $A = 8$  nuclei are underbound with the present Hamiltonian, it is premature to use these calculations as a precise test of the charge-independence-breaking components of the interaction.

### C. Isospin Mixed States

The  $(2^+;1)$  isobaric analog of the  ${}^8\text{Li}$  ground state in  ${}^8\text{Be}$  is very close in energy to the second  $(2^+;0)$  excitation, as shown in Fig. 1, and is in fact experimentally observed to be isospin-mixed with it. There are also fairly close  $(1^+;0,1)$  and  $(3^+;0,1)$  pairs at slightly higher energies in the  ${}^8\text{Be}$  spectrum. Our VMC calculations do not get the  $(2^+;0,1)$  states so close together, although the other pairs do come out quite near each other. However, we can calculate the isospin-mixing matrix elements that connect these pairs of states:

$$E_{01}(J) = \langle \Psi(J^+, 0) | H | \Psi(J^+, 1) \rangle . \quad (5.4)$$

This is done by increasing the model space to include both  $T = 0$  and  $1$  components, which corresponds to a wave function vector with 10,752 terms, and employing the same off-diagonal evaluations used to determine the  $\beta_{LS[n]}$  wave function components.

Results for the  $E_{01}(J)$  are given in Table XI. The experimental values are determined from the observed decay widths and energies [33]. The dominant contribution, from the Coulomb potential, typically accounts for less than half of the matrix element. We find the magnetic moment part of the electromagnetic interaction and the strong CSB interaction can provide a significant boost, although we still underpredict the experimental mixing by  $\sim 20\%$ . The spatial symmetry components of the different wave functions, as given in the Tables III and IV, for the  $(2^+;0,1)$  and  $(3^+;0,1)$  pairs are indeed fairly close to each other, since they have similar sizes and signs for the largest components. However, the  $(1^+;0,1)$  states are not so similar, particularly due to the large  $T = 1$   ${}^1\text{P}[31]$  component that is not

available to the  $T = 0$  state. This may be why the  $E_{01}(1)$  is noticeably smaller, which shows up through the change in sign of the magnetic moment contribution.

## VI. MOMENTS AND DENSITY DISTRIBUTIONS

The proton rms radii, magnetic moments, and quadrupole moments for the  $A = 8$  nuclear ground states are given in Table XII. The calculations have been made in impulse approximation for both the initial VMC wave function and perturbatively after GFMC constrained path propagation. Comparing the VMC and GFMC radii, it appears that the variational wave functions are a little too compact for this Hamiltonian. However, given that the present interaction underbinds these nuclei, the actual radii should be smaller than the GFMC values. Attempts have been made to determine the matter radius of  ${}^8\text{He}$  by proton-scattering experiments in inverse kinematics. Interpretation of the data is not model-independent, however, and has resulted in estimates ranging from 2.45 fm [34] to 2.6 fm [35]. The corresponding VMC and GFMC matter radii from Table XII are 2.69 fm and 2.92 fm, respectively. In the not too distant future, it may be possible to trap  ${}^8\text{He}$ ,  ${}^8\text{Li}$ , and  ${}^8\text{B}$  long enough to determine their charge radii to high precision by atomic means.

The magnetic moments of  ${}^8\text{Li}$  and  ${}^8\text{B}$  have been measured by  $\beta$ -radiation detection of implanted polarized ions [36]. Our IA calculations should be supplemented by meson-exchange currents (MEC); their contributions are dominantly isovector, and have been shown to change the magnetic moments of  ${}^3\text{H}$  and  ${}^3\text{He}$  by  $\pm 0.4 \mu_N$  [37]. The isoscalar average of the calculated magnetic moments is close the experimental value, and it is plausible that MEC contributions will bring both magnetic moments into good agreement with experiment. The quadrupole moments of  ${}^8\text{Li}$  and  ${}^8\text{B}$  have been measured by  $\beta$ -NMR and nuclear quadrupole resonance techniques [38]. The VMC and GFMC results are fairly close for  ${}^8\text{Li}$ , and just a little above the experimental value. The calculations for  ${}^8\text{B}$  are significantly further apart, despite the proton rms radii differing by only a small amount; nevertheless they bracket the experimental value. We have also calculated the hexadecapole moment for these two ground states, and find it to be consistent with 0.

One- and two-nucleon density distributions have been calculated in both VMC and GFMC. The GFMC densities are a little more spread out and less peaked than the corresponding VMC densities, as reflected in the charge radii differences; here we show only the GFMC densities. Single-nucleon density distributions for the  $A = 8$  nuclei are shown in Fig. 11; they are normalized such that the integrated value equals the appropriate total value of  $N$  or  $Z$ . The two protons in  ${}^8\text{He}$  are the most peaked distribution, which should be expected on the grounds that they are mostly confined to the  $\alpha$  core, while the six neutrons in  ${}^8\text{He}$  have the broadest distribution. The proton distribution in  ${}^8\text{Li}$  is also fairly peaked near the origin, but is broader than in  ${}^8\text{He}$  since there is one additional proton in the p-shell. The neutron distribution in  ${}^8\text{Li}$  is comparable to the  ${}^8\text{He}$  neutrons near the origin, is slightly larger in the 1-2 fm range, and then falls below at larger distances; the intermediate-range excess may be due to the significantly greater binding of  ${}^8\text{Li}$  compared to  ${}^8\text{He}$ . In contrast, the  ${}^8\text{Be}$  proton and neutron distributions are much less peaked at the origin and are rather flat out past 1 fm. This could be because  ${}^8\text{Be}$  has a significant  $2\alpha$  component in its intrinsic structure, with the two  $\alpha$ 's sitting side-by-side; as discussed in the next section.

A logarithmic plot of the single-nucleon densities for  ${}^{4,6,8}\text{He}$  isotopes is shown in Fig. 12.

The neutron halos in  ${}^6\text{He}$  and  ${}^8\text{He}$  are clearly evident, while the proton cores of these nuclei are nearly identical. The peak neutron and proton distributions in  ${}^6\text{He}$  and  ${}^8\text{He}$  are much reduced compared to  ${}^4\text{He}$ , because of the motion of the  $\alpha$  core against the center-of-mass. Two-proton density distributions for  ${}^{4,6,8}\text{He}$  are shown in Fig. 13. The relative proton-proton density in  ${}^{6,8}\text{He}$  is not effected by the motion of the  $\alpha$  relative to the center of mass; thus  $\rho_{pp}$  is an indicator of changes in the internal structure of the  $\alpha$  core in  ${}^{6,8}\text{He}$ . Here we note that there is only a small change in the  $\alpha$  core of  ${}^{6,8}\text{He}$ , i.e., about a 10% reduction in the peak compared to  ${}^4\text{He}$ , which must be compensated in the long-range tail, since the total integral under the curves is unity in each case. This reduction could be due to swelling of the  $\alpha$  core, or due to charge-exchange interactions between the protons and p-shell neutrons.

We have also calculated the single-nucleon momentum distributions shown in Fig. 14, using the VMC wave functions and the method of Ref. [39], with some algorithmic improvements. The  $N(k)$  are normalized to  $N/(2\pi)^3$  or  $Z/(2\pi)^3$ . All the distributions show a remarkably similar structure: a low-momentum core attributable to s- and p-shell orbitals, followed by a high-momentum tail beyond  $2 \text{ fm}^{-1}$  that is the sum of many small-amplitude higher-orbital contributions. This high-momentum tail is already evident in the  ${}^4\text{He}$  momentum distribution and is intimately related to the D-state of  ${}^4\text{He}$ , present due to the strong tensor forces and corresponding correlations in the wave function. The  ${}^8\text{He}$  proton distribution is very similar to that of  ${}^4\text{He}$ , showing that the  $\alpha$  core is not much altered, while the neutrons exhibit a p-shell peak near  $0.5 \text{ fm}^{-1}$ . The  ${}^8\text{Li}$  proton distribution is a little broader, as might be expected by the addition of a p-shell proton, while the neutrons show a smaller p-shell peak. The  ${}^8\text{Be}$  momentum distribution is almost exactly double that of  ${}^4\text{He}$  except at very low momenta, indicating a significant  $2\alpha$  structure.

## VII. INTRINSIC SHAPES

The ground state and first two excited states of  ${}^8\text{Be}$  have an approximate rotational energy spectrum, and are assumed to be well approximated as two  $\alpha$ 's rotating around their common center of mass. This structure is not manifest in the shell model part of the VMC wave functions, in which the  ${}^8\text{Be}$  states are constructed from an  $\alpha$ -like core surrounded by four p-shell nucleons coupled to the appropriate total angular momentum. In this section we describe an attempt to study the intrinsic structure of the  ${}^8\text{Be}$  states described by the VMC wave functions including correlations.

The standard Monte Carlo method for computing one-body densities,  $\rho(\mathbf{r})$ , is to make a random walk that samples  $|\Psi(\mathbf{r}_1, \mathbf{r}_2, \dots, \mathbf{r}_A)|^2$  and to bin  $\mathbf{r}_1, \mathbf{r}_2, \dots, \mathbf{r}_A$  for each configuration in the walk. The density is then proportional to the number of samples in each bin. In the case of a  $J = 0$  nucleus, this “laboratory” density will necessarily be spherically symmetric.

We can attempt to find the intrinsic density in body-fixed coordinates by computing the moment of inertia matrix:

$$\mathcal{M} = \sum_{i=1}^A \begin{pmatrix} x_i^2 & x_i y_i & x_i z_i \\ y_i x_i & y_i^2 & y_i z_i \\ z_i x_i & z_i y_i & z_i^2 \end{pmatrix} , \quad (7.1)$$

for each configuration. We then find the eigenvalues and eigenvectors of  $\mathcal{M}$ , rotate to those principal axes, and bin the resulting  $\mathbf{r}'_1, \mathbf{r}'_2, \dots, \mathbf{r}'_A$ . The eigenvector with the largest

eigenvalue is chosen as the  $\mathbf{z}'$  axis; further choices of the  $\pm$  direction along  $\mathbf{z}'$  and which eigenvectors to assign to  $\mathbf{y}'$  and  $\mathbf{x}'$  may also be made or averaged over. This procedure will not produce a spherically symmetric distribution, even if there is no underlying deformed structure, because almost every random configuration will have principal axes of different lengths and the rotation will always orient the longest principal axis in the  $\mathbf{z}'$  direction. We have made a number of tests using simple wave functions with no internal correlations and also nuclei like  ${}^4\text{He}$  which, in our models, should have no intrinsic deformations. We find that the projected “intrinsic” density for such cases is always prolate but that no other artificial structure is introduced.

When the above procedure is applied to the  ${}^8\text{Be}$  rotational states, a dramatic intrinsic structure is revealed. Figure 15 shows this calculation for the ground state. The figure shows contours of constant density plotted in cylindrical coordinates, with the  $z$ -axis being the axis of quantization. The calculation was made for the VMC wave function. The left side of the figure shows the standard density calculation; we can think of this as the density in the “laboratory” frame. For the  $J = 0$  ground state, this is spherically symmetric as shown. The right side of the figure shows the intrinsic density computed as described above. In this case the orientation (up or down) along  $\mathbf{z}'$  and around  $\mathbf{z}'$  ( $r = \sqrt{x^2 + y^2}$ ) was averaged over. It is clear that the intrinsic density has two peaks, with the neck between them having only one-third the peak density; we regard these as two  $\alpha$ 's.

Figure 16 shows the corresponding calculation for the  $J = 4^+$ ,  $M_J = 4$ , state of  ${}^8\text{Be}$ . In this case the the laboratory density does not have to be spherically symmetric and there is evidence of two  $\alpha$ 's rotating around the  $\mathbf{z}$  axis in the equatorial plane. The projection to the intrinsic frame rotates these to the  $\mathbf{z}'$  axis and results in an intrinsic density that is insignificantly different from that obtained for the ground state. A calculation for the  $J = 2^+$  state also produces the same intrinsic density.

These results, obtained for the VMC wave functions, suggest that the  $0^+$ ,  $2^+$ , and  $4^+$  wave functions for  ${}^8\text{Be}$  have the structure of a deformed rotor consisting of two  $\alpha$ 's. The structure is not manifest in the shell model part of the VMC wave functions; it is induced by the correlations. The optimum spatial correlations between pairs of s-shell and p-shell nucleons are similar, but those between one s-shell and one p-shell nucleon are different. Calculations using GFMC configurations give very similar results except that, especially for the  $J = 4^+$  state, the rms radius is still growing at the end of the GFMC propagation.

If the  $0^+$ ,  $2^+$ , and  $4^+$  states are generated by rotations of a common deformed structure, then their electromagnetic moments and transition strengths should all be related to the intrinsic moments. Table XIII shows the VMC computed values of the quadrupole and hexadecapole moments, and of the  $B(E2)$  and  $B(E4)$  strengths for these states. In the rotational model these are related by simple Clebsch Gordon coefficients to the intrinsic quadrupole,  $Q_0$ , or  $M_4$  moment depending on the multipolarity,  $\lambda$ . These moments are defined as

$$Q_0 = \sqrt{\frac{16\pi}{5}} \int d\mathbf{r}' \rho(\mathbf{r}') \mathbf{r}'^2 Y_{20}(\hat{\mathbf{r}}') , \quad (7.2)$$

and

$$M_4 = \int d\mathbf{r}' \rho(\mathbf{r}') \mathbf{r}'^4 Y_{40}(\hat{\mathbf{r}}') , \quad (7.3)$$

where  $\rho$  is the point proton density and  $\mathbf{r}'$  refers to the intrinsic (body-fixed) frame. The last column gives the extracted values of these intrinsic moments; we see that, with the exception  $M_4$  for the  $J = 2^+$  state, these are remarkably constant.

We can also compute values of  $Q_0$  and  $M_4$  by integrating over the projected body-fixed densities. These values might be too large because, as described above, the projection method can introduce an excessive deformation in the intrinsic shape. The values for the  $0^+$ ,  $2^+$ , and  $4^+$  states are  $Q_0 = 26.2, 27.9$ , and  $26.7$ , and  $M_4 = 55, 62, 64$ ; the  $Q_0$  are in good agreement with the values given in the Table, which were obtained from the spectroscopic quadrupole moments. We note that the ratios of these  $Q_0$  and  $M_4$  values are in reasonable agreement with the ratio obtained for a diatomic model of  ${}^8\text{Be}$  assuming two point  $\alpha$ 's separated by 4 fm.

We can attempt to project out an intrinsic structure of the  $T = 0$ ,  $J = 1^+$  and  $J = 3^+$ , states of  ${}^8\text{Be}$ . In this case we also find two peaks but of somewhat smaller density than for the  $0^+$ ,  $2^+$ , and  $4^+$  states. Clearly these peaks cannot be due to two  $\alpha$ 's rotating around each other. They presumably reflect occurrence of  $\alpha + t + p$  and  $\alpha + {}^3\text{He} + n$  structures in these states.

### VIII. CONCLUSIONS

We have made quantum Monte Carlo calculations for the ground states and low-lying excitations of  $A = 8$  nuclei interacting by realistic two- and three-nucleon potentials. These calculations have been made practical by the development of a constrained-path algorithm for the complex spatial and spin-isospin wave functions needed to describe these nuclei. This algorithm greatly reduces the “fermion-sign problem” that quantum Monte Carlo methods are subject to, allowing us to obtain binding energies for a given Hamiltonian that are accurate to 1 to 2%.

The Hamiltonian we have used, consisting of the Argonne  $v_{18}$  two-nucleon and Urbana IX three-nucleon potentials, gets the general features of the light p-shell nuclei fairly well, including the bulk of the experimentally observed binding and the correct ordering and approximate spacing of the excitation spectrum. However, with accurate calculations, we can identify specific failings of this Hamiltonian, including a few percent underbinding in  $N = Z$  nuclei, which gets progressively worse as the neutron-proton asymmetry increases, and spin-orbit splittings in the excitation spectrum that are too small. Nevertheless, we can see that the energy differences with experiment are much smaller than the magnitude of the short-range (and least-well-known) part of our three-nucleon interaction, so it is plausible that new three-nucleon force models may be able to reproduce the ground and excited states near the 1% level.

We have also been able to study energy differences between isobaric analog states and the isospin-mixing matrix elements in  ${}^8\text{Be}$ . While final conclusions should be reserved until the bulk energies are corrected by improved three-nucleon potentials, we can see that the charge-dependent and charge-symmetry-breaking components of the Argonne  $v_{18}$  potential are making significant contributions that improve the agreement with experiment.

Finally, we have also studied the moments, densities, momentum distributions, and intrinsic shapes of these nuclei. It appears that the observed static moments may be understood with our present microscopic model after we include meson-exchange current contri-

butions. We also see evidence for strong clustering in the light p-shell nuclei, particularly the  $2\alpha$  character in  $^8\text{Be}$ . This clustering is built into the variational wave functions by the strong pair correlations, which depend upon the nucleon orbits and seem to be preserved in the GFMC propagation.

With the present method, and the continuing rapid increases in computational power that massively parallel machines are bringing, we are confident that we will be able to extend our calculations to the  $A = 9, 10$  nuclei in the near future, and to  $^{12}\text{C}$  in a few year's time.

## ACKNOWLEDGMENTS

The authors thank Dr. Dieter Kurath for many useful suggestions. The many-body calculations were made possible by generous grants of time on the IBM SP and SGI Origin 2000 of the Mathematics and Computer Science Division, Argonne National Laboratory. The GFMC calculations of  $^8\text{Li}$  excited states were made with early-user time on the IBM SP at the National Energy Research Scientific Center. The work of SCP and RBW is supported by the U. S. Department of Energy, Nuclear Physics Division, under contract No. W-31-109-ENG-38, that of JC by the U.S. Department of Energy under contract W-7405-ENG-36, and that of VRP by the U.S. National Science Foundation via grant PHY98-00978.

## REFERENCES

- \* Electronic address: wiringa@anl.gov
- † Electronic address: spieper@anl.gov
- ‡ Electronic address: carlson@lanl.gov
- § Electronic address: vrp@uiuc.edu
- [1] B. S. Pudliner, V. R. Pandharipande, J. Carlson, S. C. Pieper, and R. B. Wiringa, Phys. Rev. C **56**, 1720 (1997).
- [2] R. B. Wiringa, Nucl. Phys. **A631**, 70c (1998); S. C. Pieper in *Microscopic Quantum Many-Body Theories and Their Applications*, edited by J. Navarro and A. Polls, (Springer, Berlin, 1998), p. 337; S. C. Pieper in *ENAM 98, Exotic Nuclei and Atomic Masses*, edited by B. M. Sherrill, D. J. Morrissey, and C. N. Davids, (AIP, Woodbury, 1998), p. 399; V. R. Pandharipande, Nucl. Phys. **A654**, 157c (1999).
- [3] R. B. Wiringa, V. G. J. Stoks, and R. Schiavilla, Phys. Rev. C **51**, 38 (1995).
- [4] B. S. Pudliner, V. R. Pandharipande, J. Carlson, and R. B. Wiringa, Phys. Rev. Lett. **74**, 4396 (1995).
- [5] J. Carlson, V. R. Pandharipande, and R. B. Wiringa, Nucl. Phys. **A401**, 59 (1983).
- [6] R. B. Wiringa, Rev. Mod. Phys. **65**, 231 (1993).
- [7] R. B. Wiringa and R. Schiavilla, Phys. Rev. Lett. **81**, 4317 (1998).
- [8] L. Lapikás, J. Wesseling and R. B. Wiringa, Phys. Rev. Lett. **82**, 4404 (1999).
- [9] A. Arriaga, V. R. Pandharipande, and R. B. Wiringa, Phys. Rev. C **52**, 2362 (1995).
- [10] R. B. Wiringa, Phys. Rev. C **43**, 1585 (1991).
- [11] S. Cohen and D. Kurath, Nucl. Phys. **73**, 1 (1965).
- [12] A. Bohr and B. R. Mottelson, *Nuclear Structure Volume I*, App. 1C, (W. A. Benjamin, New York, 1969).
- [13] F. Ajzenberg-Selove, Nucl. Phys. **A490**, 1 (1988).
- [14] A. A. Korsheninnikov, *et al.*, Phys. Lett. B **316**, 38 (1993); W. von Oertzen, *et al.*, Nucl. Phys. **A588**, 129c (1995); Th. Stolla, *et al.*, Z. Phys. A **356**, 233 (1996).
- [15] J. A. Carlson and R. B. Wiringa, in *Computational Nuclear Physics 1*, edited by K. Langanke, J. A. Maruhn, and S. E. Koonin (Springer Verlag, Berlin, 1991).
- [16] B. S. Pudliner, University of Illinois Thesis (1996).
- [17] R. Schiavilla, V. R. Pandharipande, and A. Fabrocini, Phys. Rev. C **40**, 1484 (1989).
- [18] S. Zhang, J. Carlson, and J. E. Gubernatis, Phys. Rev. Lett. **74**, 3652 (1995).
- [19] S. Zhang, J. Carlson, and J. E. Gubernatis, Phys. Rev. B **55**, 7464 (1997).
- [20] D. M. Ceperley and M. H. Kalos, in *Monte Carlo Methods in Statistical Physics*, edited by K. Binder (Springer-Verlag, Heidelberg, 1979).
- [21] M. H. Kalos, D. Levesque, and L. Verlet, Phys. Rev. A **9**, 2178 (1974).
- [22] R. Blankenbecler, D. J. Scalapino, and R. L. Sugar, Phys. Rev. D**24**, 2278 (1981).
- [23] J. B. Anderson, J. Chem. Phys. **63**, 1499 (1975); **65**, 4122 (1976).
- [24] D. M. Ceperley and B. J. Alder, Phys. Rev. Lett. **45**, 566 (1980).
- [25] J. W. Moskowitz, K. E. Schmidt, M. A. Lee, and M. H. Kalos, J. Chem. Phys. **77**, 349 (1982).
- [26] P. J. Reynolds, D. M. Ceperley, B. J. Alder, and W. A. Lester, J. Chem. Phys. **77**, 5593 (1982).
- [27] J. Carlson, J. E. Gubernatis, G. Ortiz, and S. Zhang, Phys. Rev. B **59**, 12788 (1999).
- [28] S. Sorella, Phys. Rev. Lett. **80**, 4458 (1998).

- [29] B. S. Pudliner, A. Smerzi, J. Carlson, V. R. Pandharipande, S. C. Pieper, and D. G. Ravenhall, Phys. Rev. Lett. **76**, 2416 (1996).
- [30] J. Carlson, V. R. Pandharipande, and R. B. Wiringa, Nucl. Phys. **A424**, 47 (1984).
- [31] M. Peshkin, Phys. Rev. **121**, 636 (1960).
- [32] W. Benenson and E. Kashy, Rev. Mod. Phys. **51**, 527 (1979).
- [33] F. C. Barker, Nucl. Phys. **83**, 418 (1966).
- [34] G. D. Alkhazov, *et al.*, Phys. Rev. Lett. **78**, 2313 (1997).
- [35] J. S. Al-Khalili and J. A. Tostevin, Phys. Rev. C **57**, 1846 (1998).
- [36] P. Raghavan, At. Data Nucl. Data Tables **42**, 189 (1989).
- [37] R. Schiavilla, V. R. Pandharipande, and D. O. Riska, Phys. Rev. C **40**, 2294 (1989).
- [38] N. Stone, [www.nndc.bnl.gov/nndc/stone\\_moments/moments.html](http://www.nndc.bnl.gov/nndc/stone_moments/moments.html) (1997).
- [39] R. Schiavilla, V. R. Pandharipande, and R. B. Wiringa, Nucl. Phys. **A449**, 219-242 (1986).

TABLES

TABLE I. Values of variational parameters in p-shell nuclei; in the expression for  $V_p$ ,  $L$  is the total orbital angular momentum.

$2S+1L[n]$	$^1L[4]$	$^{1,3}L[31]$	$^{1,3}L[22]$	$^3L[211]$
$c_{sp}$	0.85	0.85	0.85	0.85
$d_{sp}$ (fm)	3.2	3.2	3.2	3.2
$c_{pp}^{[n]}$	0.1	0.2	0.3	0.4
$d_{pp}$ (fm)	3.2	3.2	3.2	3.2
$V_p$ (MeV)	$-20.0+L$	$-20.0+L$	$-20.0+L$	$-20.0+L$
$R_p$ (fm)	4.0	4.0	4.0	4.0
$a_p$ (fm)	1.5	1.5	1.5	1.5

TABLE II.  $\beta_{LS[n]}$  components for  $^8\text{He}$  states, listed in order of increasing excitation.

$(J^\pi; T)$	$^1S[22]$	$^1D[22]$	$^3P[211]$
$(0^+; 2)$	0.842		-0.539
$(2^+; 2)$		0.958	-0.287
$(1^+; 2)$			1
$(0^+; 2)$	0.546		0.838
$(2^+; 2)$		0.294	0.956

TABLE III.  $\beta_{LS[n]}$  components for  $^8\text{Li}$  states, listed in order of increasing excitation.

$(J^\pi; T)$	$^3P[31]$	$^3D[31]$	$^3F[31]$	$^1P[31]$	$^1D[31]$	$^1F[31]$	$^3S[22]$	$^3D[22]$
$(2^+; 1)$	0.936	-0.289	-0.121		0.118			-0.104
$(1^+; 1)$	0.740	-0.334		0.576			-0.067	-0.068
$(0^+; 1)$	1							
$(3^+; 1)$		0.912	0.275			-0.296		-0.067
$(2^+; 1)$	0.343	0.854	0.386		0.046			0.047
$(1^+; 1)$	0.644	0.410		-0.618			-0.162	-0.091
$(1^+; 1)$	-0.036	0.812		0.531			-0.229	0.063
$(4^+; 1)$			1					
$(2^+; 1)$	-0.111	-0.260	0.550		0.780			-0.101
$(3^+; 1)$		-0.269	0.922			0.037		-0.275

TABLE IV.  $\beta_{LS[n]}$  components for  ${}^8\text{Be}$  states, listed in order of increasing excitation.

$(J^\pi; T)$	${}^1\text{S}[4]$	${}^1\text{D}[4]$	${}^1\text{G}[4]$	${}^3\text{P}[31]$	${}^3\text{D}[31]$	${}^3\text{F}[31]$
$(0^+; 0)$	0.997			-0.076		
$(2^+; 0)$		0.999		0.033	0.037	-0.018
$(4^+; 0)$			0.997			0.079
$(2^+; 0)$		-0.019		0.948	-0.314	0.045
$(1^+; 0)$				0.861	0.508	
$(1^+; 0)$				-0.526	0.850	
$(3^+; 0)$					0.891	0.453
$(4^+; 0)$			-0.089			0.996
$(2^+; 0)$		-0.038		0.270	0.844	0.463
$(3^+; 0)$					-0.457	0.889
$(0^+; 0)$	0.098			0.995		

 TABLE V.  ${}^6\text{Li}(\text{gs})$  results (in MeV) using different three-body propagators.

Propagator	$\langle V^{2\pi, A} \rangle$	$\langle V^{2\pi, C} \rangle$	$\langle H \rangle$
$G$	-8.6(2)	-5.2(1)	-31.25(12)
$\tilde{G}, n = 1$	-8.5(2)	-5.2(1)	-31.15(11)
$\tilde{G}, n = 4$	-8.9(2)	-5.3(1)	-31.23(7)
$\tilde{G}, n = \infty$	-8.8(2)	-5.2(1)	-31.25(12)
just two-body	-5.8(2)	-3.9(1)	-29.86(23)

TABLE VI. Scaling of calculation with system size

	$A$	$P = A(A - 1)/2$	$2^A \times I(A, T)$	$\Pi(\times {}^8\text{Be})$
${}^4\text{He}$	4	6	$16 \times 2$	0.001
${}^5\text{He}$	5	10	$32 \times 5$	0.010
${}^6\text{Li}$	6	15	$64 \times 5$	0.036
${}^7\text{Li}$	7	21	$128 \times 14$	0.33
${}^8\text{Be}$	8	28	$256 \times 14$	1
${}^8\text{He}$	8	28	$256 \times 20$	1.4
${}^8\text{Li}$	8	28	$256 \times 28$	2
${}^9\text{Be}$	9	36	$512 \times 42$	8.7
${}^{10}\text{B}$	10	45	$1024 \times 42$	24
${}^{11}\text{B}$	11	55	$2048 \times 132$	200
${}^{12}\text{C}$	12	66	$4096 \times 132$	530
${}^8\text{n}$	8	28	$256 \times 1$	0.071
${}^{14}\text{n}$	14	91	$16384 \times 1$	26

TABLE VII. Experimental and quantum Monte Carlo energies of  $A=2-8$  nuclear ground states in MeV.

$^A Z(J^\pi; T)$	VMC ( $\Psi_T$ )	VMC ( $\Psi_V$ )	GFMC	Expt
$^2 \text{H}(1^+; 0)$	-2.2248(5)			-2.2246
$^3 \text{H}(\frac{1}{2}^+; \frac{1}{2})$	-8.15(1)	-8.32(1)	-8.47(1)	-8.48
$^4 \text{He}(0^+; 0)$	-26.97(3)	-27.78(3)	-28.34(4)	-28.30
$^6 \text{He}(0^+; 1)$	-23.64(7)	-24.87(7)	-28.11(9)	-29.27
$^6 \text{Li}(1^+; 0)$	-27.10(7)	-27.83(5)	-31.15(11)	-31.99
$^7 \text{He}(\frac{3}{2}^-; \frac{3}{2})$	-18.05(11)	-19.75(12)	-25.79(16)	-28.82
$^7 \text{Li}(\frac{3}{2}^-; \frac{1}{2})$	-31.92(11)	-33.04(7)	-37.78(14)	-39.24
$^8 \text{He}(0^+; 2)$	-17.98(8)	-19.31(12)	-27.16(16)	-31.41
$^8 \text{Li}(2^+; 1)$	-28.00(14)	-29.76(13)	-38.01(19)	-41.28
$^8 \text{Be}(0^+; 0)$	-45.47(16)	-46.79(19)	-54.44(19)	-56.50

TABLE VIII. VMC, GFMC, and experimental excitation energies (adjusted to their respective ground states) in MeV. Numbers in parentheses are Monte Carlo error estimates for theory, and uncertainties in the energy for experiment. We also give experimental widths where known in keV (except where otherwise noted). The  $^8\text{Be}$  states marked with an \* are isospin-mixed.

$^A Z(J^\pi; T)$	VMC (MeV)	GFMC (MeV)	Expt (MeV)	$\Gamma$ (keV)
$^8\text{He}(2^+; 2)$	2.22(16)	3.01(23)	3.59	
$^8\text{He}(1^+; 2)$	3.32(17)	4.42(25)		
$^8\text{He}(0^+; 2)$	4.72(18)			
$^8\text{He}(2^+; 2)$	5.01(17)			
$^8\text{Li}(1^+; 1)$	1.34(18)	0.57(24)	0.98	12(4) fs
$^8\text{Li}(0^+; 1)$	2.83(19)	1.91(29)		
$^8\text{Li}(3^+; 1)$	3.35(18)	2.66(28)	2.26	33(6)
$^8\text{Li}(2^+; 1)$	3.86(18)			
$^8\text{Li}(1^+; 1)$	4.22(19)		3.21	$\approx 1000$
$^8\text{Li}(1^+; 1)$	5.32(19)		5.4	$\approx 650$
$^8\text{Li}(4^+; 1)$	6.08(18)	6.27(31)	6.53	35(15)
$^8\text{Li}(2^+; 1)$	6.20(18)			
$^8\text{Li}(3^+; 1)$	7.31(18)		6.1	$\approx 1000$
$^8\text{Li}(0^+; 2)$	11.24(18)	12.10(25)	10.82	< 12
$^8\text{Be}(2^+; 0)$	2.39(25)	2.91(25)	3.04(3)	1500(20)
$^8\text{Be}(4^+; 0)$	9.95(24)	9.58(27)	11.4(3)	$\approx 3500$
$^8\text{Be}(2^+; 1)$	18.60(23)	18.02(27)	16.63*	108(1)
$^8\text{Be}(2^+; 0)$	20.29(24)		16.92*	74(1)
$^8\text{Be}(1^+; 1)$	19.89(23)		17.64	11(1)
$^8\text{Be}(1^+; 0)$	20.03(23)	18.09(33)	18.15	138(6)
$^8\text{Be}(1^+; 0)$	21.73(24)			
$^8\text{Be}(3^+; 1)$	21.77(22)		19.07	270(20)
$^8\text{Be}(3^+; 0)$	21.85(24)	19.53(33)	19.24	230(30)
$^8\text{Be}(4^+; 0)$	25.85(22)		19.86	700(100)
$^8\text{Be}(2^+; 0)$	23.61(23)		20.1	$\approx 1100$
$^8\text{Be}(3^+; 0)$	25.53(23)			
$^8\text{Be}(0^+; 0)$	28.62(26)		20.2	< 1000
$^8\text{Be}(0^+; 2)$	29.55(22)	29.93(25)	27.49	5.5(2.0)

TABLE IX. Kinetic and potential energy contributions to GFMC energies in MeV.

$^A Z(J^\pi; T)$	$K$	$v_{ij}$	$V_{ijk}$	$v_{ij}^\gamma$	$v_{ij}^\pi$	$V_{ijk}^{2\pi}$	$V_{ijk}^R$
$^2\text{H}(1^+; 0)$	19.81	-22.04		0.018	-21.28		
$^3\text{H}(\frac{1}{2}^+; \frac{1}{2})$	51.2(3)	-58.9(3)	-1.2(0)	0.04(0)	-45.0(2)	-2.2(0)	1.0(0)
$^4\text{He}(0^+; 0)$	110.7(7)	-135.3(7)	-6.3(1)	0.86(0)	-102.4(5)	-11.5(1)	5.2(1)
$^6\text{He}(0^+; 1)$	138.(1)	-164.(1)	-7.0(1)	0.86(0)	-119.(1)	-13.1(2)	6.1(2)
$^6\text{Li}(1^+; 0)$	153.(1)	-183.(1)	-7.3(2)	1.68(1)	-143.(1)	-13.6(2)	6.3(2)
$^7\text{He}(\frac{3}{2}^-; \frac{3}{2})$	156.(2)	-183.(2)	-8.1(2)	0.87(0)	-131.(1)	-15.2(4)	7.2(3)
$^7\text{Li}(\frac{3}{2}^-; \frac{1}{2})$	190.(2)	-227.(2)	-9.1(2)	1.77(1)	-172.(1)	-17.9(3)	8.8(2)
$^8\text{He}(0^+; 2)$	166.(1)	-195.(1)	-8.0(2)	0.87(0)	-135.(1)	-15.8(2)	7.8(2)
$^8\text{Li}(2^+; 1)$	217.(2)	-257.(2)	-10.2(2)	1.86(1)	-192.(1)	-20.8(4)	10.6(3)
$^8\text{Be}(0^+; 0)$	248.(2)	-301.(2)	-14.9(3)	3.27(1)	-227.(1)	-27.1(4)	12.3(3)

 TABLE X. VMC and GFMC isovector and isotensor energy coefficients  $a_{A,T}^{(n)}$  in keV.

$a_{A,T}^{(n)}$	$K^{CSB}$		$v^\gamma$		$v^{CSB} + v^{CD}$		Total		
	VMC	GFMC	VMC	GFMC	VMC	GFMC	VMC	GFMC	Expt.
$a_{8,1}^{(1)}$	24	20	1689	1586	66	63	1779(4)	1669(7)	1770
$a_{8,1}^{(2)}$	0	0	155	132	-11	3	144(4)	135(7)	145
$a_{8,2}^{(1)}$	17	15	1478	1423	40	47	1535(3)	1485(5)	1659
$a_{8,2}^{(2)}$	0	0	140	129	26	29	166(4)	158(4)	153

 TABLE XI. VMC isospin-mixing matrix elements for  $^8\text{Be}$  in keV

$J^\pi$	$v^{\text{Coul}}$	$v^{\text{MM}}$	$v^{\text{CSB}}$	$K^{\text{CSB}}$	$E_{01}$	Expt.
$2^+$	63	18	26	2	109(4)	149
$1^+$	40	-1	15	1	55(2)	120
$3^+$	33	15	13	1	62(2)	63

 TABLE XII. VMC and GFMC values for point proton rms radii (in fm), for magnetic moments (in  $\mu_N$ ), and quadrupole moments (in  $\text{fm}^2$ ) in impulse approximation. In the GFMC calculations, the rms radii of the two excited states of  $^8\text{Be}$  are steadily growing with propagation time.

	$\langle r_p^2 \rangle^{1/2}$		$\mu$		Expt.	VMC	$Q$		$\langle r_p^4 Y_{40} \rangle$
	VMC	GFMC	VMC	GFMC			VMC	GFMC	
$^8\text{He}(0^+; 2)$	1.91(1)	1.98(1)							
$^8\text{Li}(2^+; 1)$	2.21(2)	2.18(2)	1.12(1)	1.3(1)	1.653	3.2(1)	3.6(2)	3.19(7)	0.1(2)
$^8\text{Be}(0^+; 0)$	2.25(1)	2.48(1)							
$^8\text{B}(2^+; 1)$	2.47(3)	2.57(1)	1.46(1)	1.4(2)	1.036	5.5(2)	7.9(4)	6.83(21)	0.7(8)
$^8\text{C}(0^+; 2)$	2.90(4)	3.17(1)							

TABLE XIII. VMC calculation of moments and transition strengths for different multipolarities,  $\lambda$ , in the rotational states of  ${}^8\text{Be}$ ; the units are fm and the proton charge.

Observable	$\lambda$	Value	$Q_0$ or $M_4$
$Q(2^+)$	2	$-7.61(8)$	$26.6(3)$
$Q(4^+)$	2	$-9.76(10)$	$26.8(3)$
$B(E2, 2^+ \rightarrow 0^+)$	2	$14.8(4)$	$27.3(4)$
$B(E2, 4^+ \rightarrow 2^+)$	2	$18.2(4)$	$25.3(3)$
$\langle 2^+, 2   r^4 Y_{4,0}   2^+, 2 \rangle$	4	$2.5(2)$	$53.(4)$
$\langle 4^+, 4   r^4 Y_{4,0}   4^+, 4 \rangle$	4	$4.3(2)$	$34.(2)$
$B(E4, 4^+ \rightarrow 0^+)$	4	$167.(16)$	$39.(2)$

## FIGURES

FIG. 1. The experimental spectrum for  $A = 8$  nuclei. All narrow low-lying states are shown, as well as the wide rotational states in  ${}^8\text{Be}$ . Higher-lying and negative parity states in  ${}^8\text{Be}$  and some wider states in  ${}^8\text{Li}$  are not shown.

FIG. 2. Constrained and unconstrained propagation tests for  ${}^6\text{Li}(\text{gs})$ . See the text for a description of the symbols.

FIG. 3. Constrained and unconstrained propagation tests for an eight-neutron drop. See the text for a description of the symbols.

FIG. 4. Constrained and unconstrained propagation tests for  ${}^8\text{He}(\text{gs})$ . See the text for a description of the symbols.

FIG. 5. Constrained propagation to large  $\tau$  for states of  ${}^6\text{Li}$ .

FIG. 6. GFMC  $E(\tau)$  for states of  ${}^8\text{Be}$ . The solid lines show the averages of the last 7 values; the dashed lines show the corresponding statistical errors.

FIG. 7. GFMC  $E(\tau)$  for states of  ${}^8\text{Li}$ .

FIG. 8. GFMC  $E(\tau)$  for states of  ${}^8\text{He}$ .

FIG. 9. VMC, GFMC, and experimental energies of nuclear states for  $4 \leq A \leq 8$ . The light shading shows the Monte Carlo statistical errors or experimental uncertainties.

FIG. 10. VMC, GFMC, and experimental excitation energies of nuclear states for  $6 \leq A \leq 8$

FIG. 11. The neutron and proton densities in  ${}^8\text{He}$ ,  ${}^8\text{Li}$ , and  ${}^8\text{Be}$ .

FIG. 12. The neutron and proton densities in  ${}^4\text{He}$ ,  ${}^6\text{He}$ , and  ${}^8\text{He}$ , shown on a logarithmic scale.

FIG. 13. The proton-proton densities in  ${}^4\text{He}$ ,  ${}^6\text{He}$ , and  ${}^8\text{He}$ .

FIG. 14. The neutron and proton momentum distributions in  ${}^8\text{He}$ ,  ${}^8\text{Li}$ , and  ${}^8\text{Be}$ .

FIG. 15. Contours of constant density, plotted in cylindrical coordinates, for  ${}^8\text{Be}(0^+)$ . The left side is in the “laboratory” frame while the right side is in the intrinsic frame.

FIG. 16. Contours of constant density for  ${}^8\text{Be}(4^+)$ .

Fig. 1 (Wiringa, et al.)

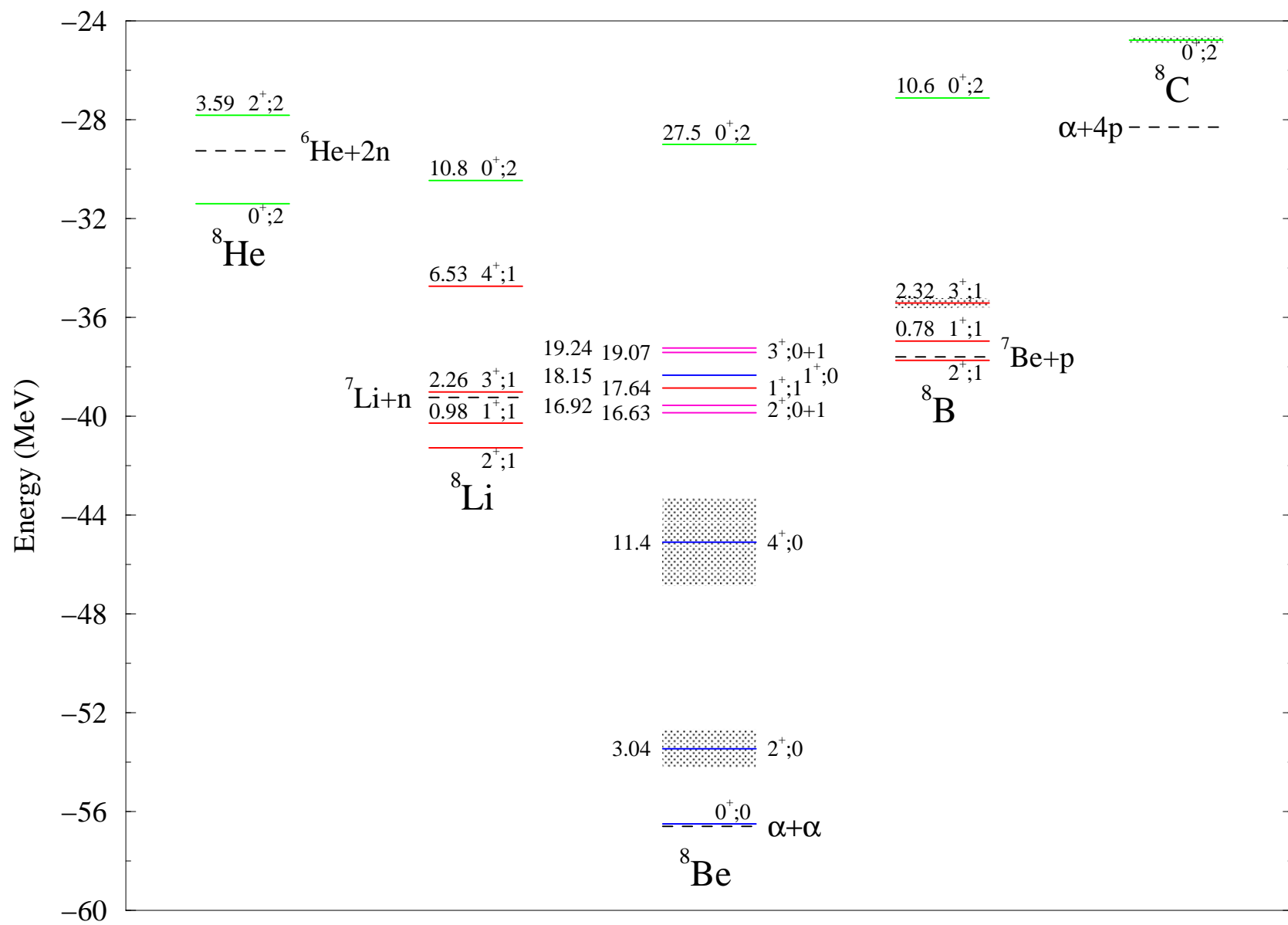


Fig. 2 (Wiringa, et al.)

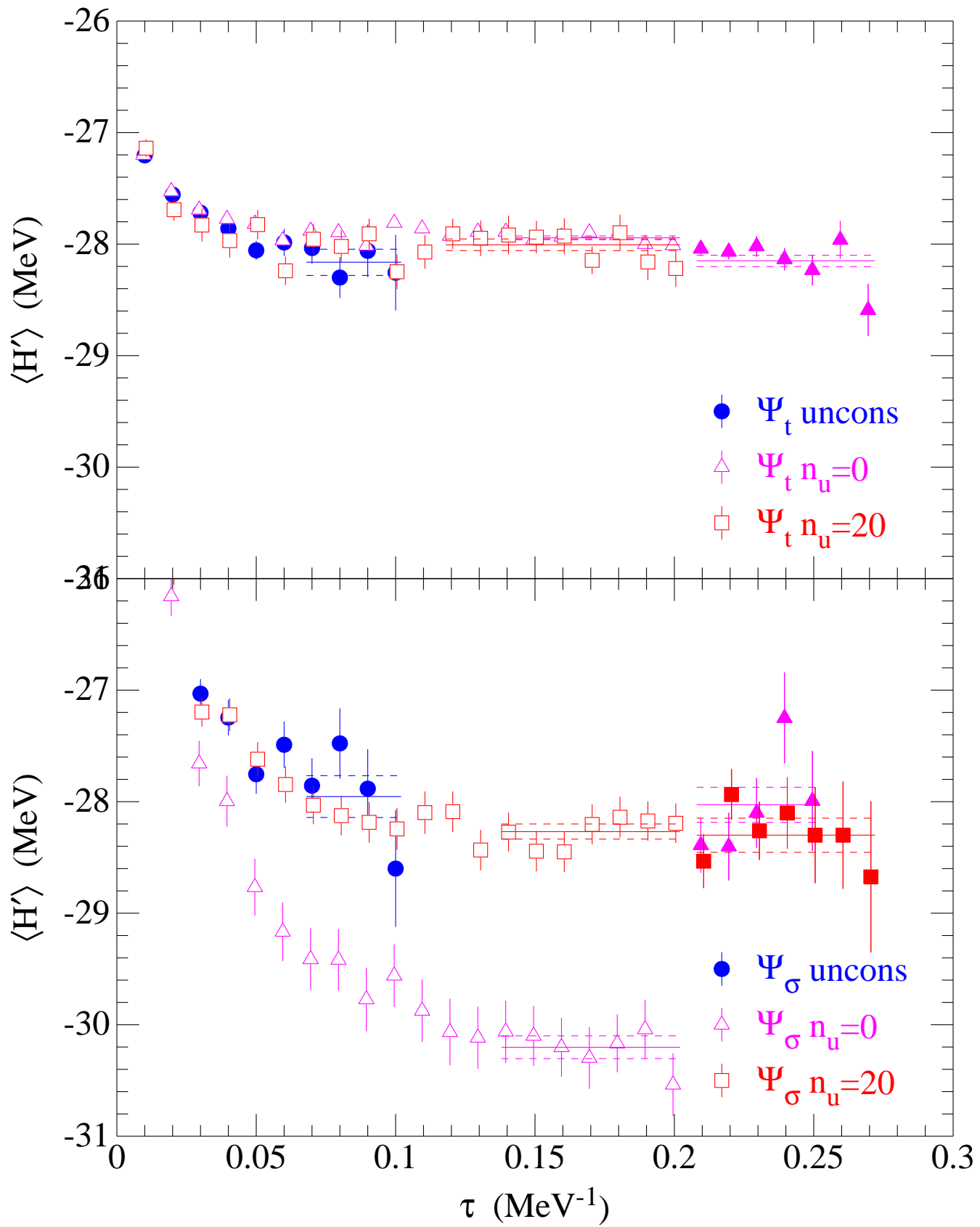


Fig. 3 (Wiringa, et al.)

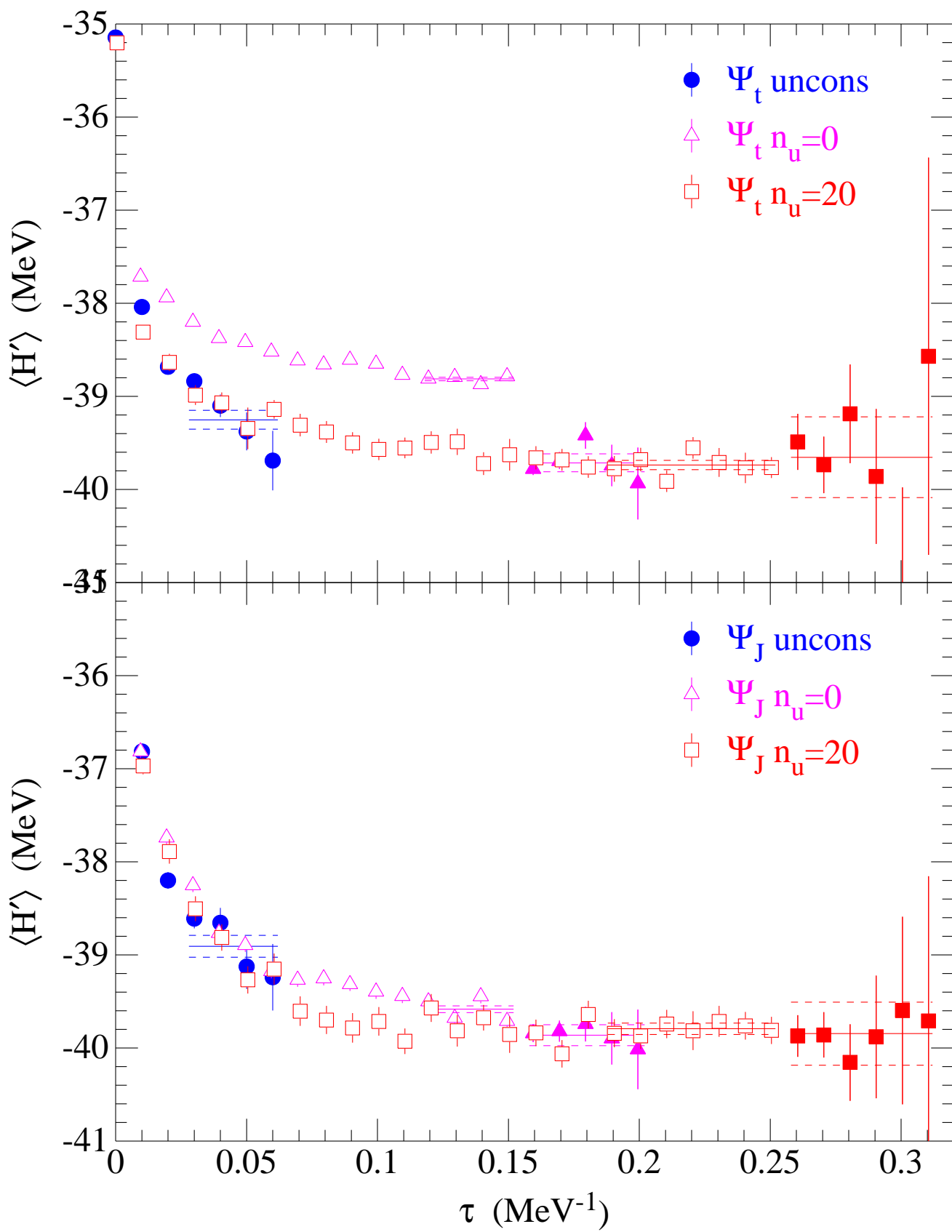
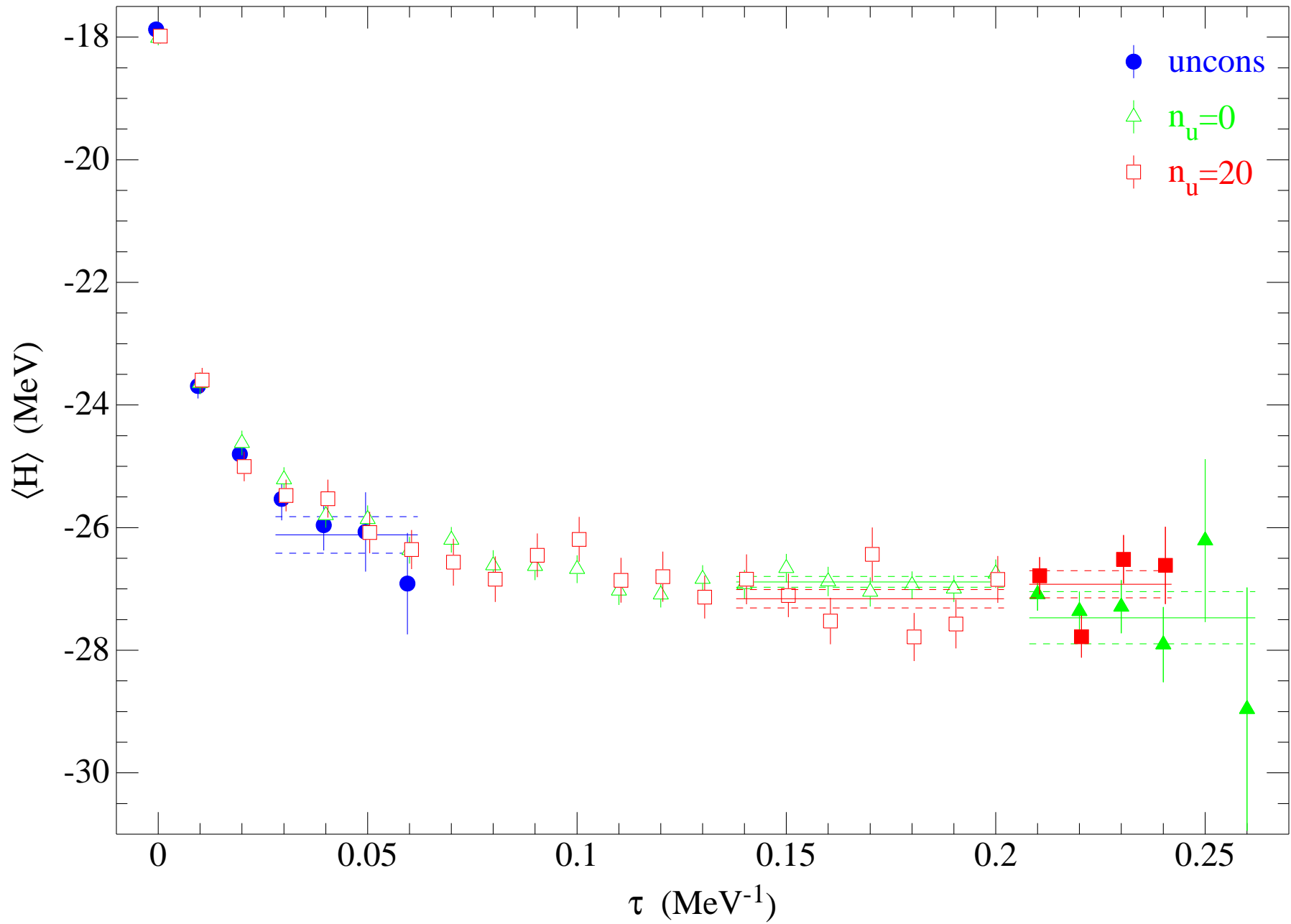


Fig. 4 (Wiringa, et al.)



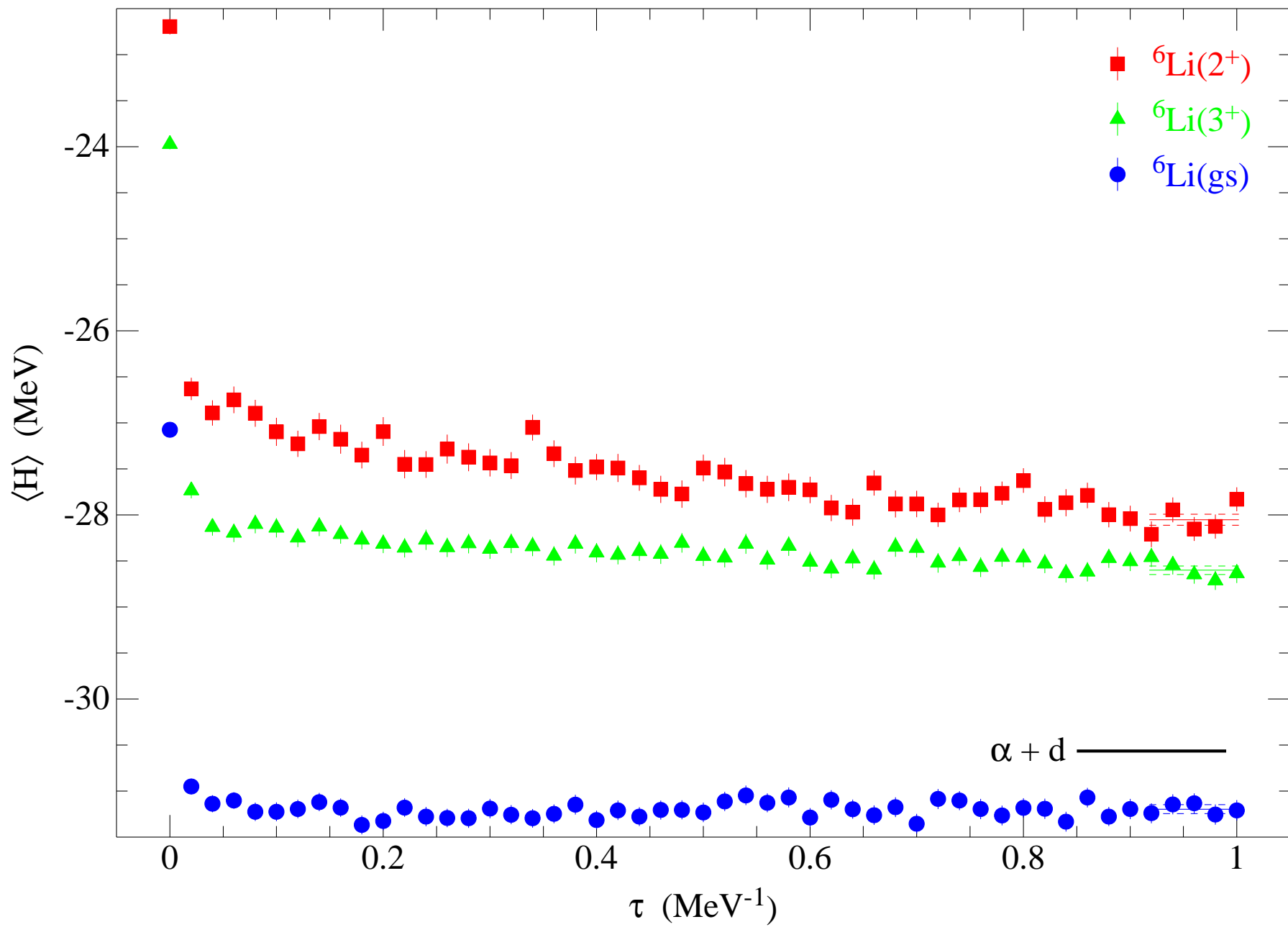


Fig. 5 (Wiringa, et al.)

Fig. 6 (Wiringa, et al.)

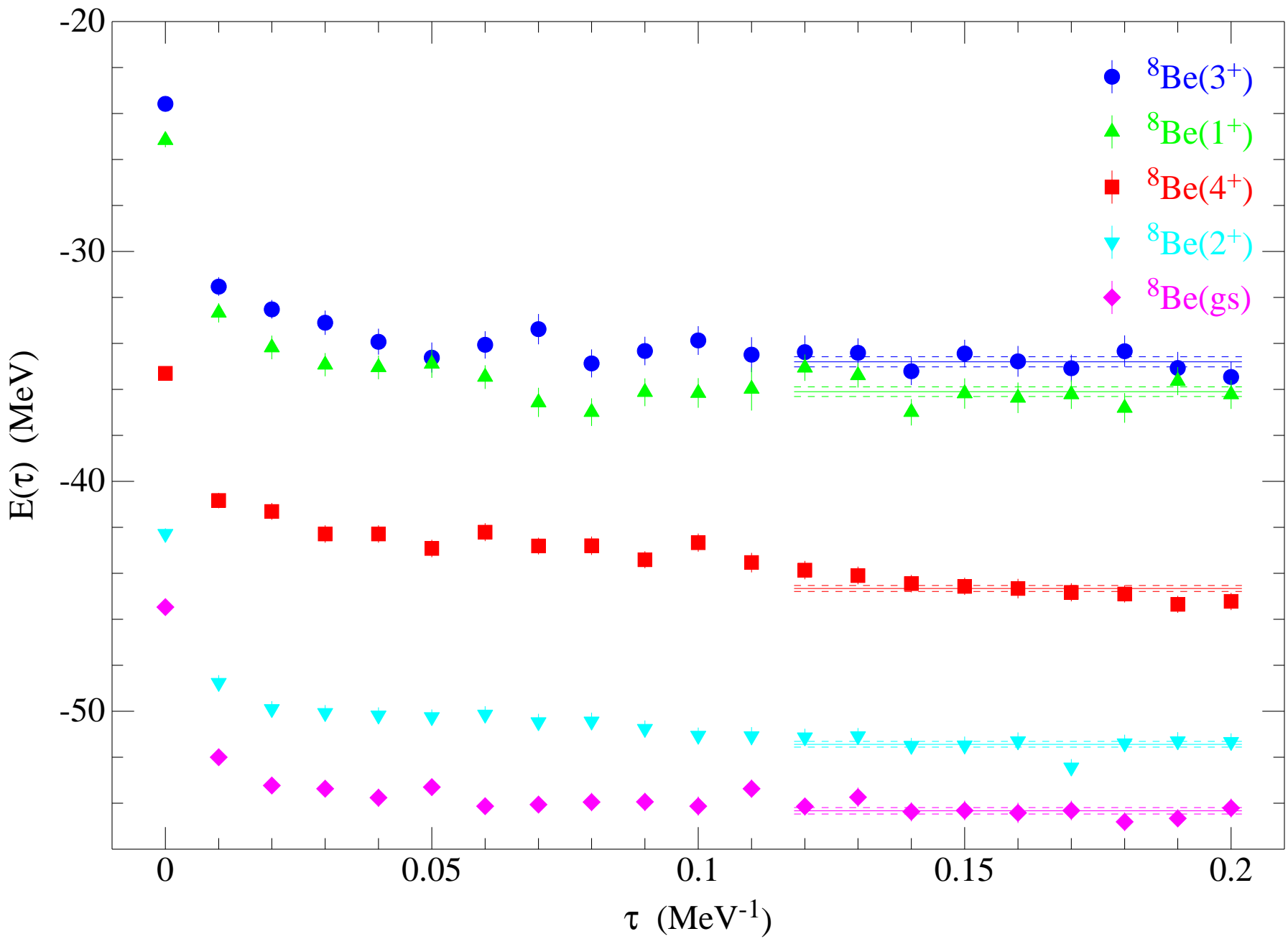


Fig. 7 (Wiringa, et al.)

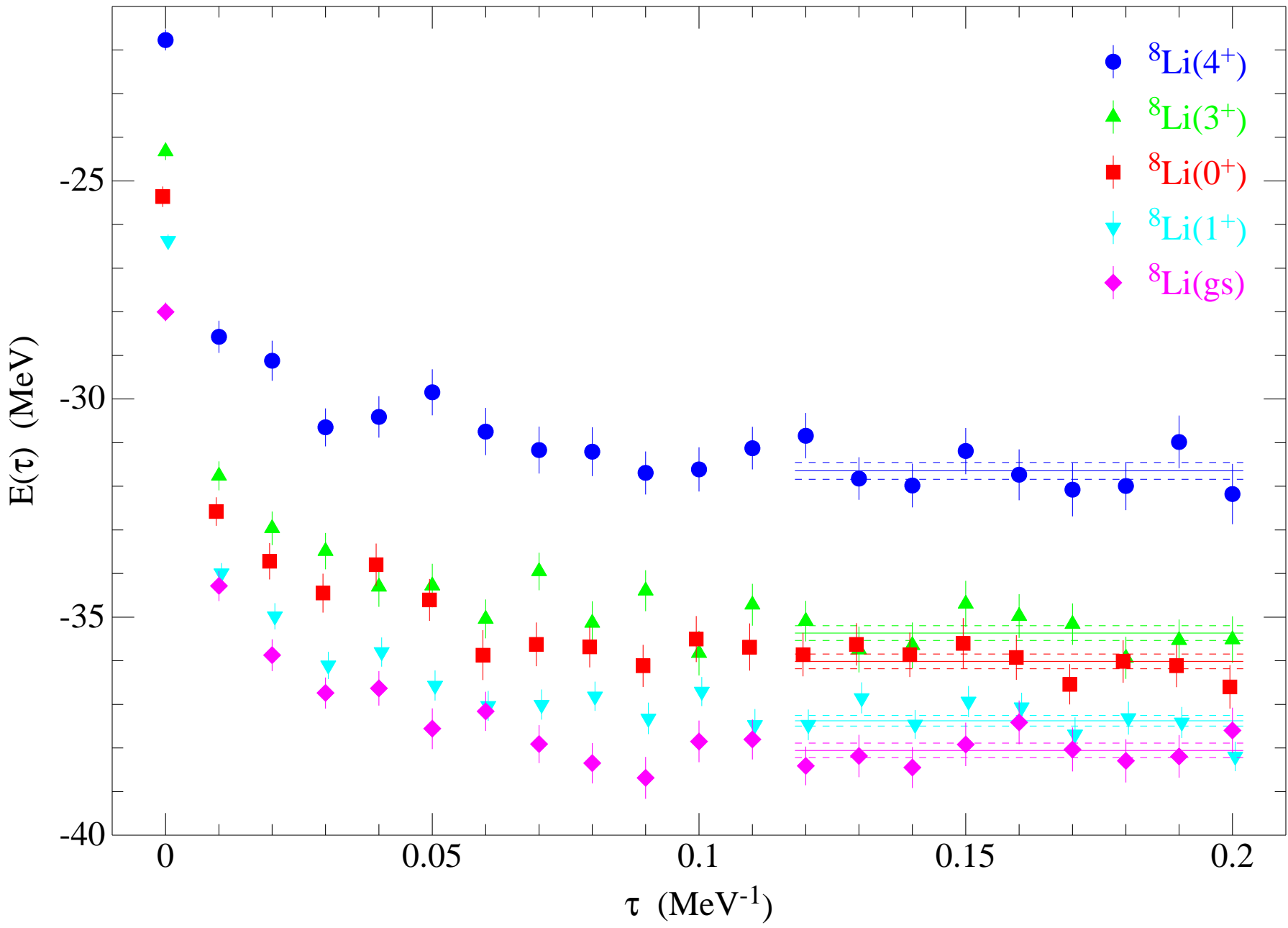
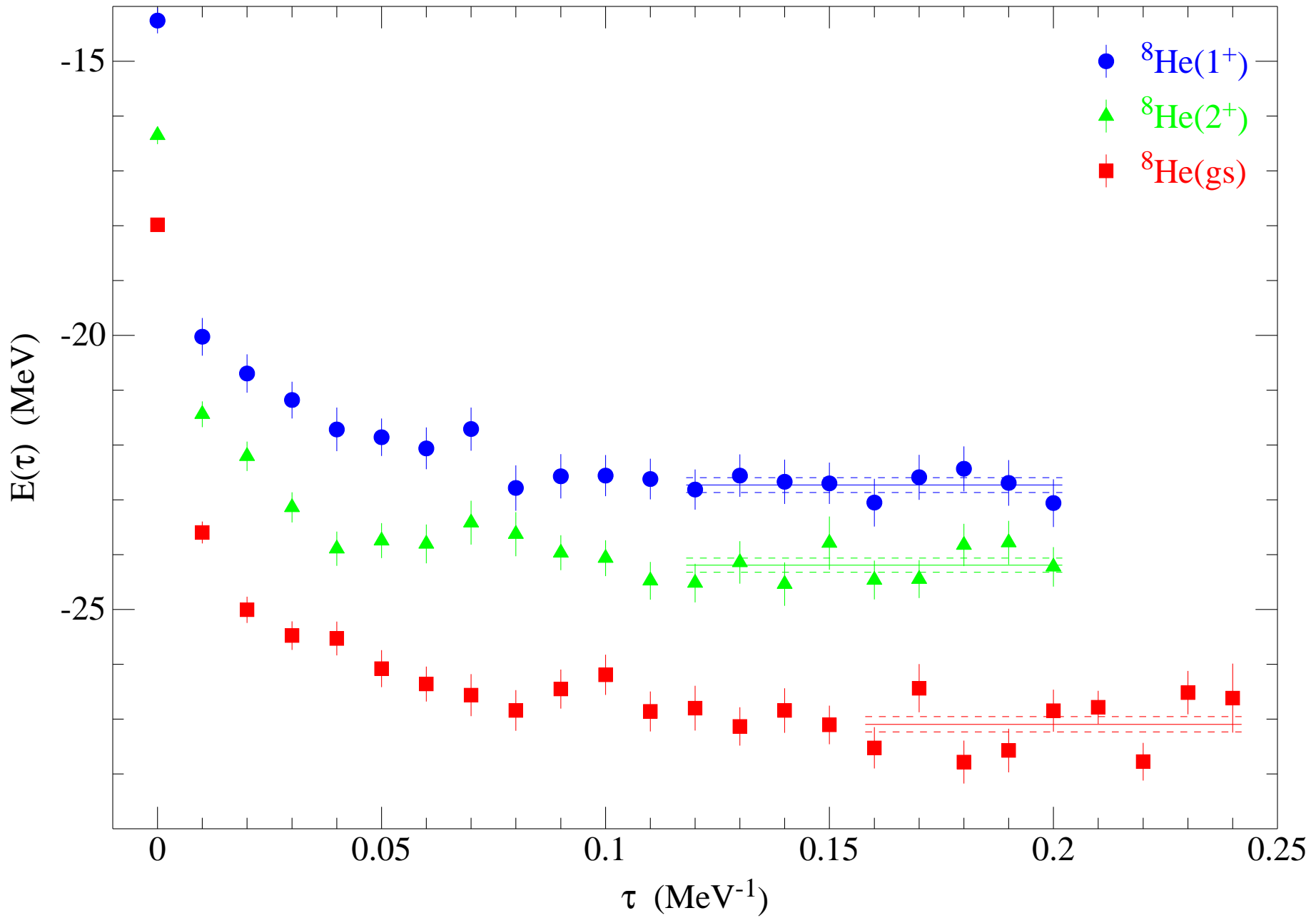


Fig. 8 (Wiringa, et al.)



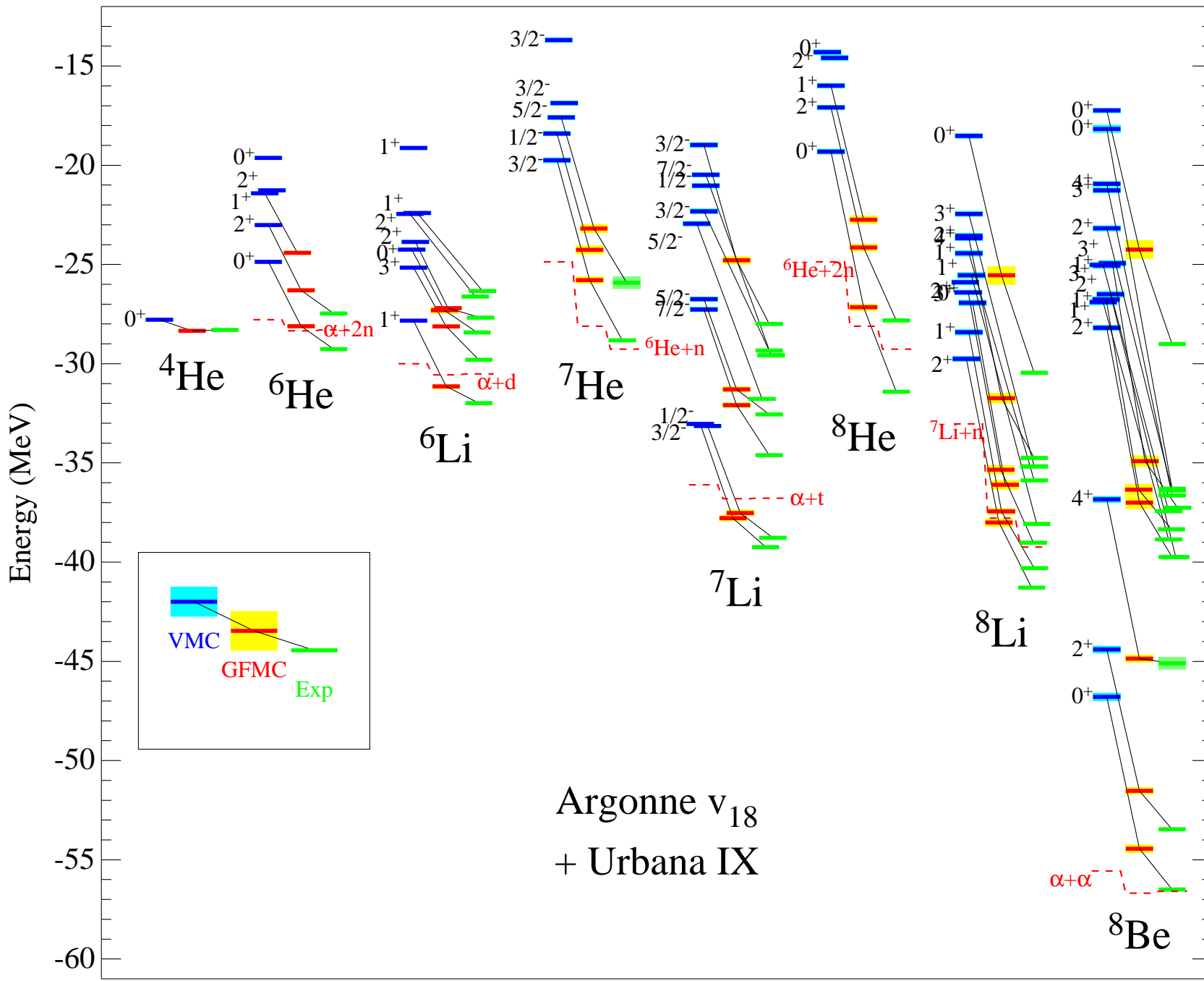


Fig. 9 (Wiringa, et al.)

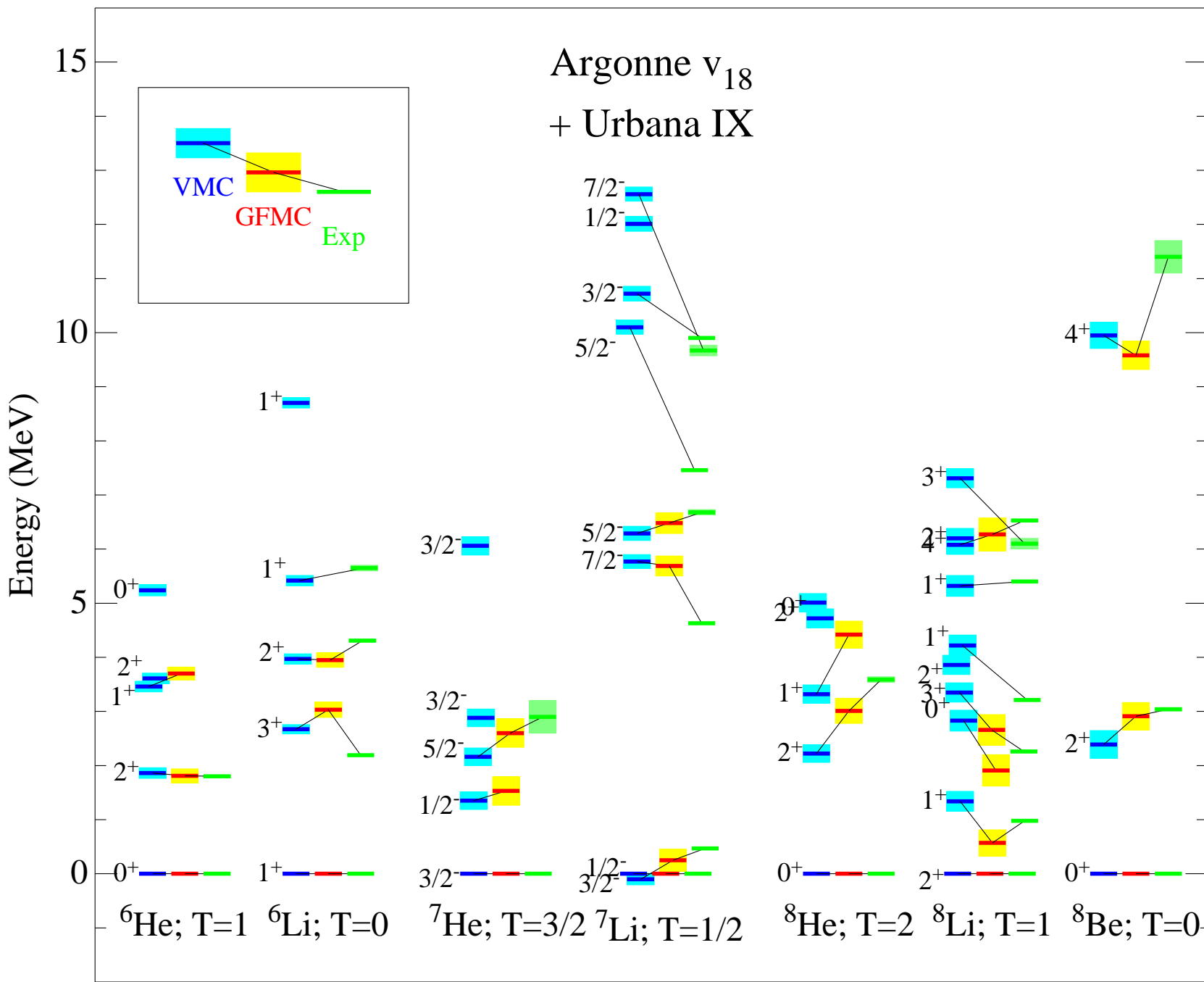


Fig. 10 (Wiringa, et al.)

Fig. 11 (Wiringa, et al.)

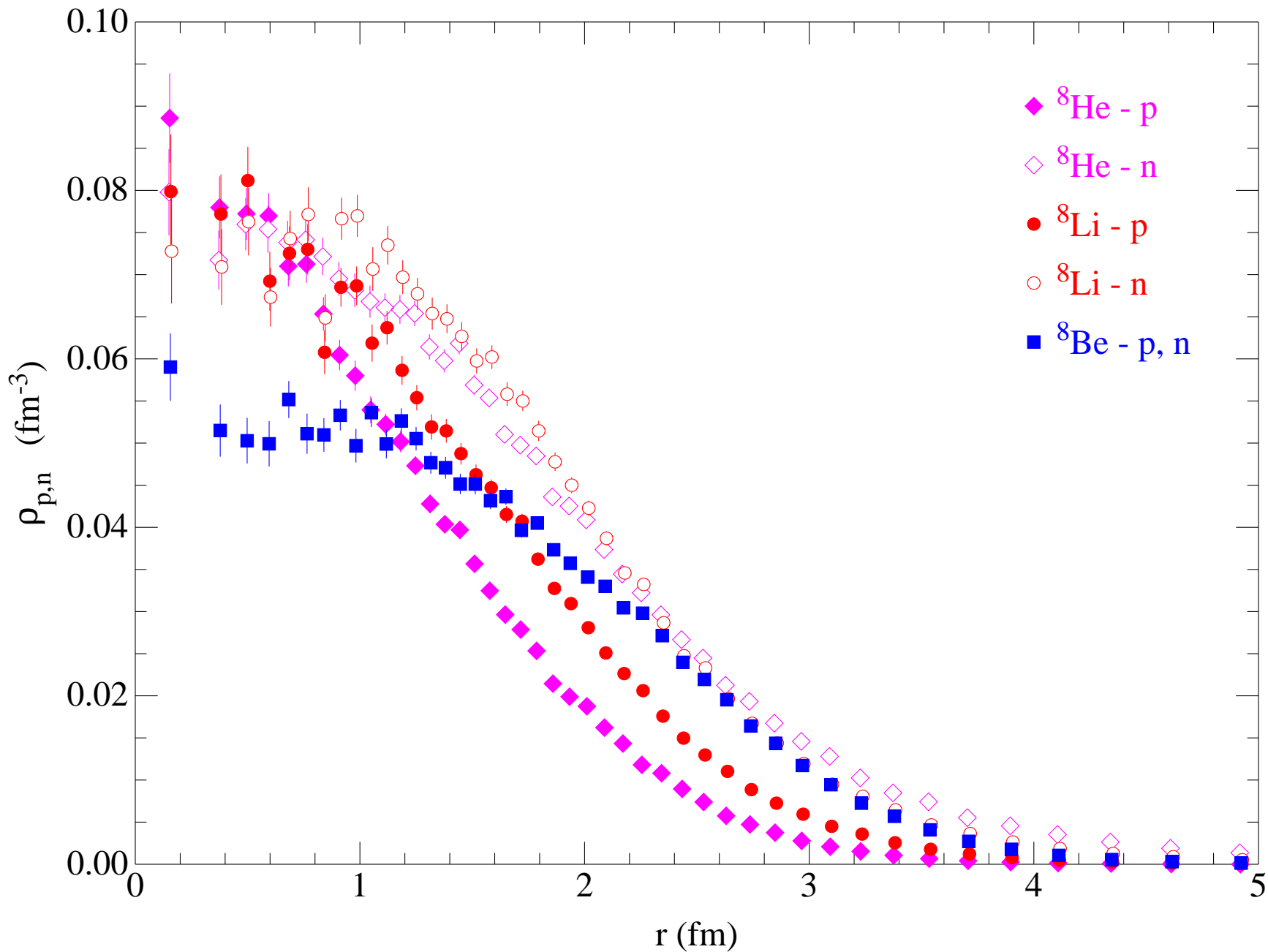


Fig. 12 (Wiringa, et al.)

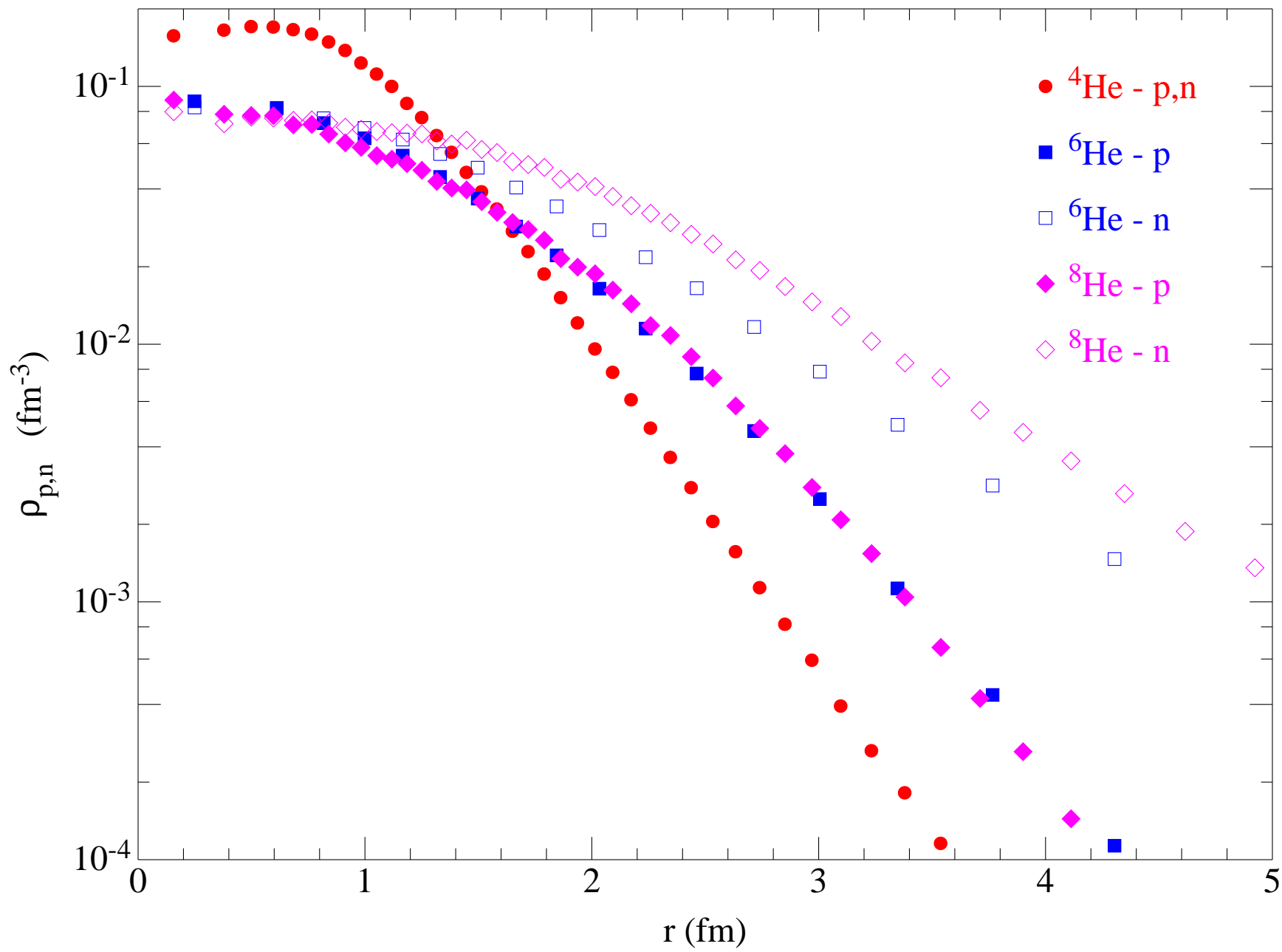
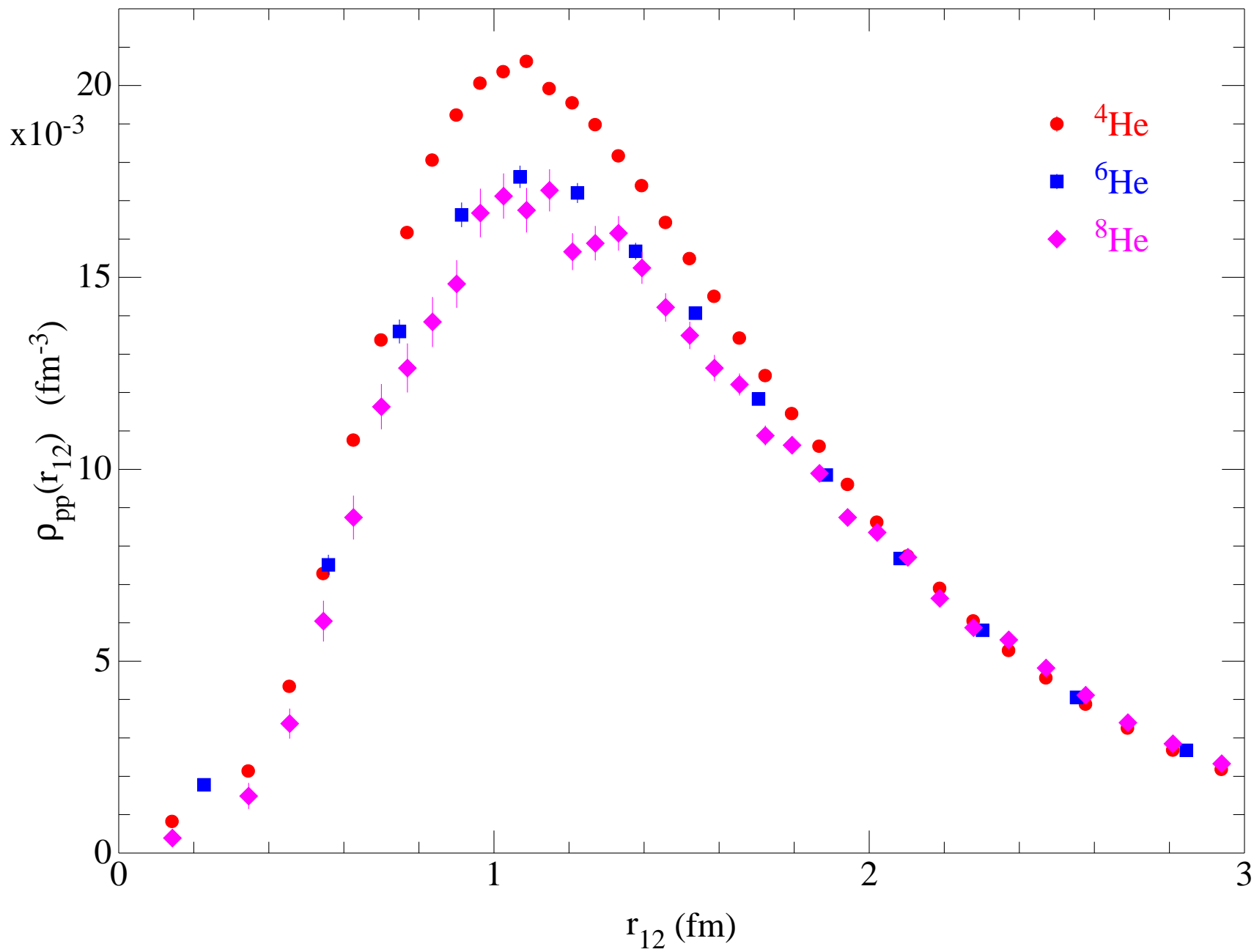


Fig. 13 (Wiringa, et al.)



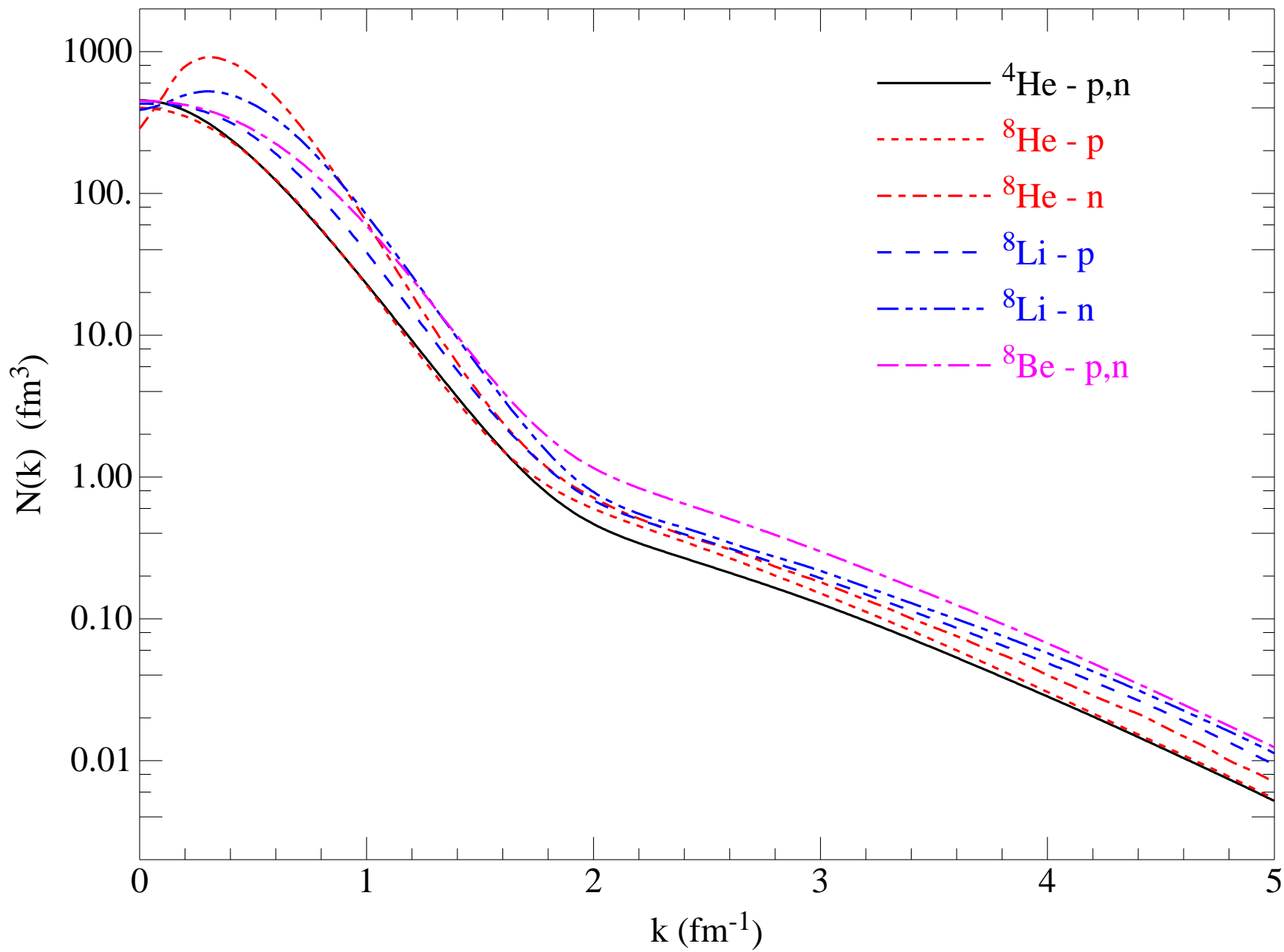


Fig. 14 (Wiringa, et al.)

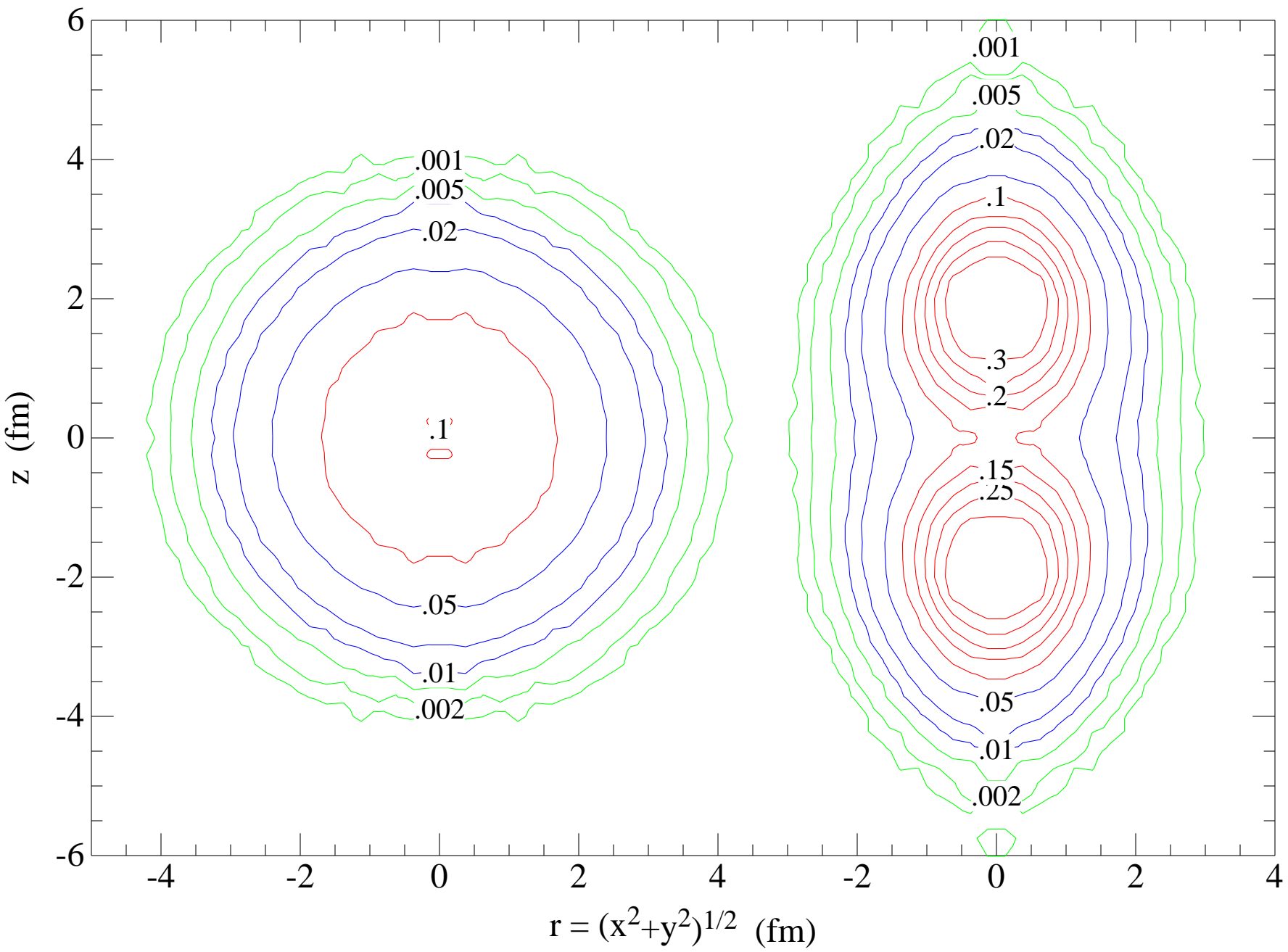


Fig. 15 (Wiringa, et al.)

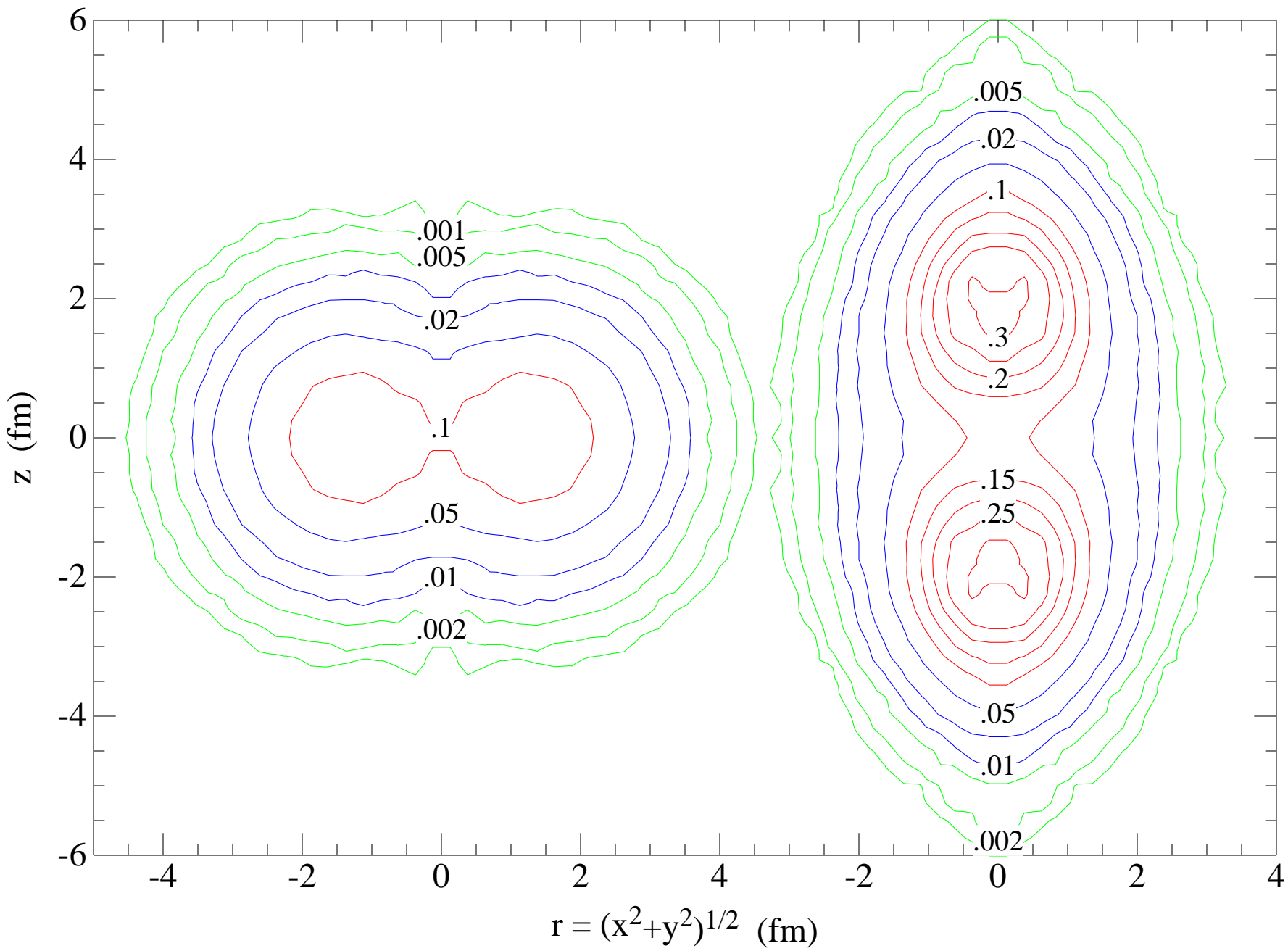


Fig. 16 (Wiringa, et al.)